One-Pot tandem catalysis: Green synthesis of β-pinene derivatives with MgO and mesoporous catalysts

Luis A. Gallego-Villada [*], Edwin A. Alarcón [*], Felipe Bustamante, Aída Luz Villa

Environmental Catalysis Research Group, Chemical Engineering Department, Universidad de Antioquia, Medellín, Colombia

ARTICLE INFO

ABSTRACT

Metal-modified heterogeneous catalysts based on mesoporous supports such as MCM-41 and SBA-15 were prepared and evaluated in the one-pot tandem transformation of β-pinene, along with MgO. This route involves epoxidation with H_2O_2 followed by the subsequent isomerization of the epoxide, yielding myrtanal as the major product; this aldehyde has wide-ranging applications as a fine chemical in fragrances, flavors, and as a precursor for pharmaceutical products. Several metals (Sn, Fe, Cu, Co) were anchored onto the supports by wetness impregnation methodology and the solids were thoroughly characterized using ICP/OES, XRD, N_2 physisorption, TEM-EDX, pyridine-FTIR, NH_3-TPD, and XPS techniques. Among these catalysts, Fe (5.07 wt%)/SBA-15 (FeS1) exhibited the highest yield to myrtanal (63 %) with a H_2O_2 efficiency of up to 60 %; this catalyst had a total acidity of 138 µmol g^{-1}, a surface area of 496 m^2 g^{-1}, a pore volume of 0.96 cm^3 g^{-1}, and an acid site density of 0.28 µmol m^{-2}. Myrtanal selectivity was also high with Sn-based catalysts, while it was poor with Cu-based materials and the null activity of Co catalysts. Total Lewis acidity and acid site density were identified as suitable kinetic descriptors of catalytic data, owing to their crucial role in the ring-opening of monoterpene epoxides. The most active catalyst showed reusability without considerable loss of substrate conversion or selectivity towards myrtanal. Additionally, no leaching of Fe was observed. Based on materials characterization and catalytic results, a plausible reaction pathway was proposed for the one-pot tandem transformation of β-pinene towards myrtanal.

1. Introduction

The fine chemistry industry stands as a pivotal sector, crucial for the production of targeted molecules utilized as precursors in fragrances, pharmaceuticals, drugs, and related compounds [1,2]. Synthesizing these products entails working on small scales of production, typically around 10,000 metric tons per year. Despite their relatively modest volume, these chemicals command high unit prices compared to others, owing to their exceptional purity, exceeding 99 % with less than 10 ppm of metal residues, and stringent quality requirements, with pharmaceuticals often requiring an enantiomeric excess exceeding 98 % [3]. Terpenes and terpenoids represent the most abundant and diverse class of natural products, exceeding 75,000 variants, often found within essential oils (EOs), which are volatile and concentrated liquids extracted from various plant parts [4,5]. Monoterpenes and sesquiterpenes typically dominate the composition of EOs; for instance, turpentine oil, predominantly comprising α-pinene and β-pinene, is extracted

from the raw resin obtained through steam distillation of pine trees [6]. Notably, the chemical composition of turpentine varies significantly based on factors such as wood species, biomass growth region, pulping process or mill, and even harvesting season [7].

The oxidation of monoterpenes over heterogeneous catalysts has been widely investigated, focusing on two competitive routes; the first one corresponds to typical oxidation by radical pathways using oxidizing agents, while the second one is associated with the epoxidation of the C=C bond to achieve the corresponding cyclic ether [3]. The predominance of each reaction pathway depends on the olefin nature, the oxidizing agent, the catalyst, and the reaction conditions. Bioderived biomass such as β-pinene monoterpene has gained tremendous importance nowadays as it can be converted to β-pinene epoxide (Fig. 1), which is an important chemical used in the production of polymers, fragrances, formulations in manufacturing, pharmaceuticals, and cosmetics, among others [8,9]. However, as β-pinene epoxide is a highly strained molecule, it can be rearranged under mild conditions into

---

* Corresponding authors.
   E-mail addresses: alfonso.gallego@udea.edu.co (L.A. Gallego-Villada), edwin.alarcon@udea.edu.co (E.A. Alarcón).
   URL: https://orcid.org/0000-0001-6415-3178 (L.A. Gallego-Villada), https://orcid.org/0000-0001-5887-4016 (E.A. Alarcón).
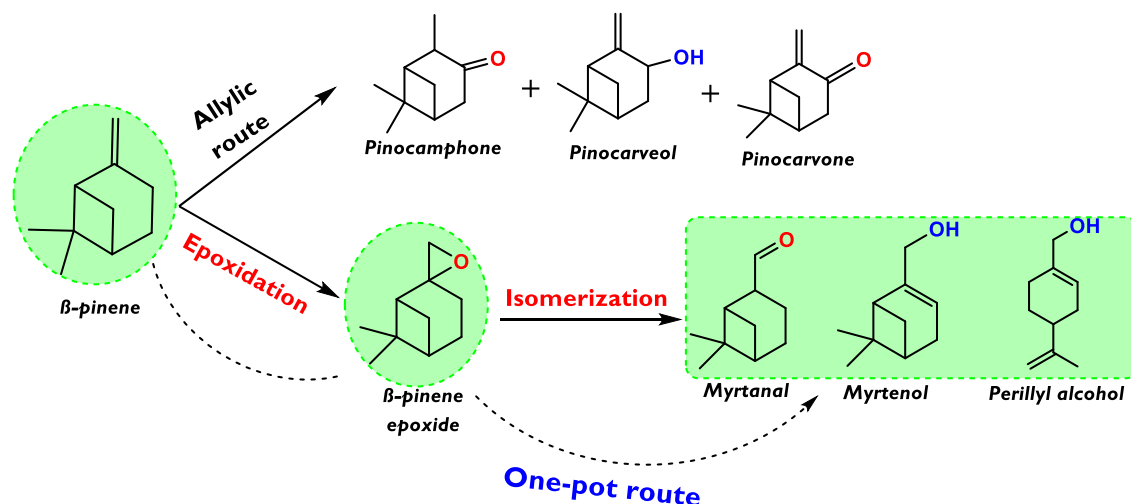
Fig. 1. Reaction pathways of the β-pinene transformation towards isomers of β-pinene epoxide.

Table 1
Heterogeneous catalytic systems for the oxidation/epoxidation of β-pinene.

Entry	Catalyst	Reaction conditions	Oxidizing agent	X_β (%)	S_i (%)	Ref.
1	ZnCo-MOF	30 mg catalyst, 3 mmol substrate, 10 g DMF, 90 °C, 5 h	40 mL min^{-1} air	70.8	62.5 Epoxide	[8]
2	CoO$_X$/mordenite	100 mg of catalyst, 6 mmol of substrate, 10 g of DMF, 90 °C, 4 h	40 mL min^{-1} air and 0.6 mmol CHP	36.8	93.3 Epoxide	[12]
3	MoCl$_2$O$_2$Bipy/TiO$_2$-NT	15 mg catalyst, 0.1 mmol substrate, 10 mL CH$_3$CN, 19 °C, 18 h, light λ = 360 nm.	O$_2$	46	72 Epoxide 18 Myrtenal	[13]
4	ZSM-5/Co-MOF	10 mg catalyst, 3 mmol substrate, 10 g DMF, 90 °C, 5 h	40 mL min^{-1} air and 0.3 mmol CHP	72.6	78.3 Epoxide	[14]
5	[Co(NH$_3$)$_6$]Cl$_3$	5 mg catalyst, 3 mmol substrate, 10 g, 90 °C, 5 h,	40 mL min^{-1} air and 0.3 mmol TBHP	43	55 Epoxide	[15]
6	FeCl$_3$·6H$_2$O	25 mg catalyst, 0.5 mmol substrate, 9 mL t-amyl alcohol, 25 °C	1.5 mmol H$_2$O$_2$	91.0	>50 Epoxide	[19]
7	PdCl$_2$	100 μmol catalyst, 2.5 mmol substrate, 10 mL CH$_3$CN, 60 °C, 8 h	3 mmol H$_2$O$_2$	58	19 Epoxide 57 Pinocarveol 24 Pinocarvone	[20]
8			9 mmol H$_2$O$_2$	55	4 Epoxide 47 Pinocarveol 49 Pinocarvone	
9	[LMn(O)$_3$MnL] (PF$_6$)$_2$	1.25 μmol catalyst, 1.25 mmol substrate, 5 mL CH$_3$CN, 25 °C, 0.5 h	6.25 mmol H$_2$O$_2$	NR	10 Epoxide [a]	[21]
10	Pd/HPA-300/SBA-15	15 mg catalyst, 1 mmol substrate, 1 mL acetone, 50 °C, 18 h	6.8 mmol H$_2$O$_2$	99	63 Pinocarveol 12 Pinocamphone 16 Myrtenol	[22]
11	Pd(0.5)/HPA-SBA-15			90	67 Pinocarveol 13 Pinocamphone 15 Myrtenol	
12	MgO	1: 1.2: 30.2: 19.7: 3.2: 15.6 wt ratios for β-pinene: MgO: H$_2$O: acetone: H$_2$O$_2$: acetonitrile, 50 °C, 2 h.	H$_2$O$_2$	100	74 Epoxide	[17]
13	[(nBu$_3$Sn)$_2$MoO$_4$]	30 mg catalyst, 5 mmol substrate, 10 mL CH$_3$CN, 50 °C, 10 h	10 mmol UHP	40	70 Epoxide 11 Pinocamphone 9 Pinocarveol	[23]

X$_\beta$: β-Pinene conversion. **S$_i$:** Selectivity to product i. **DMF:** Dimethylformamide. **CHP:** Cumene hydroperoxide. **UHP:** Urea hydroperoxide. **Bipy:** 2,2′ −bipyridine-4,4′ −dicarboxylato. **NR:** Not reported. [a]Value corresponds to the yield.

thermodynamically more stable compounds such as myrtanal, myrtenol, or perillyl alcohol (Fig. 1). These products have a wide variety of applications in the fine chemistry industry such as fragrances, flavors, precursors of pharmaceutical products, and diesel additives [10,11].

Table 1 presents some heterogeneous catalysts that have been reported for the oxidation/epoxidation of β-pinene using different oxidizing agents such as molecular oxygen (O$_2$), hydrogen peroxide (H$_2$O$_2$), *tert*-butyl hydroperoxide (TBHP), cumene hydroperoxide (CHP), and urea hydroperoxide (UHP). Entries 1–5 (Table 1) show that air or O$_2$ was the oxidizing agent in the epoxidation with catalysts such as ZnCo-

MOF [8], CoO$_X$/mordenite [12], MoCl$_2$O$_2$Bipy/TiO$_2$-NT [13], ZSM-5/Co-MOF [14], and [Co(NH$_3$)$_6$]Cl$_3$ [15]. The highest yield to β-pinene epoxide (56.8 %), using O$_2$ as an oxidant and CHP as the initiator, was achieved with the ZSM-5/Co-MOF composite catalyst (entry 4), resulting also in a highly active material for the epoxidation of α-pinene and R-(+)-limonene with yields to the epoxides of 94.5 % and 47.1 %, respectively. These results suggest a dependence of the reactivity on the monoterpene structure, due to the presence of a bicyclic structure in pinenes, favoring the reactivity in comparison with limonene.

On the other hand, from an environmental point of view, H$_2$O$_2$ is

convenient because it generates water as a byproduct [9]. However, for safety reasons, H_2O_2 is often available commercially in aqueous solutions (30 wt%), whose water content can have a significant effect as a real inhibitor of catalysts by metals, slowing down the reaction. In general, the epoxide selectivity is poor in the presence of water or protic solvents due to the ring-opening secondary reaction leading to the formation of glycol compounds [16]. Therefore, it is an important challenge to investigate optimal reaction conditions to avoid undesirable reactions and maximize the selectivity to the target molecules. Many systems have used H_2O_2 as the oxidizing agent (entries 6–12, Table 1), with MgO (entry 12) standing out as the significantly superior catalyst for the epoxidation of β-pinene, achieving complete conversion and 74 % selectivity to the epoxide after 2 h and at a very low temperature (50 °C) [17]. This catalyst is used in a Payne system consisting of the formation of an epoxidizing agent like peroxyacetimidic acid from H_2O_2 using acetonitrile as the activator, acetone as solvent, and water as an improver [17]. This catalytic system has also been employed for the versatile epoxidation of R-(+)-limonene, yielding either limonene epoxides (endo and exo) or limonene diepoxide, depending on the reaction conditions [18]. With UHP as an oxidizing agent and an organotin-oxometalate coordination polymer, $[(nBu_3Sn)_2MoO_4]$, as catalyst (entry 13), a significantly low conversion (40 %) was achieved after a long reaction time (10 h).

In the context of β-pinene epoxide isomerization, various heterogeneous catalysts have been investigated. Among them, one notable catalyst is a microporous and crystalline material characterized by pores with a diameter of at least 0.52 nm [24,25], whose empirical formula is $H_w(M_wTi_xSn_yZr_zSi_{1-w-x-z})O_2$; this catalyst exhibited a remarkable 98 % conversion and 94 % selectivity towards myrtanal (80 °C, 1 h, acetonitrile as solvent). In addition, mesoporous catalysts based on Me/MCM-41 (Me = Sn, Ti, Zr, Al, and Si) have been also explored. Notably, Sn/MCM-41 emerged as the most effective catalyst, achieving complete conversion with 82 % selectivity towards myrtanal, 4 % to myrtenol, and 5 % to perillyl alcohol (80 °C, 1 h, nitromethane as solvent) [11]. It has been suggested that Sn enhances acidity strength and Lewis behavior required for myrtanal synthesis. Other catalysts reported in the literature include Sn-β [26], supported ionic liquid [27], Sn-MCM-41 [28], Fe-β zeolite [29], and tetraimidazolium nitrate ([PEimi][HNO_3]_4) [30]. Therefore, experimental findings have indicated that myrtanal formation is favored by Lewis acidity, particularly in non-polar solvents like toluene.

Consequently, the production of myrtanal using β-pinene as a starting material has been carried out through two independent stages. Firstly, β-pinene epoxide is obtained in one reactor, which is then purified to obtain high-purity epoxide. Subsequently, it is used as a substrate for the epoxide rearrangement in another reaction vessel to obtain the target molecules, either myrtanal, myrtenol, or perillyl alcohol. However, a significant contemporary challenge in organic chemistry is the search for alternative cleaner, safer, and environmentally friendly technologies [31], which are aimed at contributing to the goals of sustainable development and the principles of green chemistry. Therefore, the reduction of waste, together with the use of renewable feedstock, environmentally friendly reagents, and catalysts, is significant to achieving more sustainable processes [31]. An effective approach is to synthesize myrtanal as the target molecule in a single reaction vessel, which is directly related to the 'one-pot' concept, being able to apply to a multi-step reaction, method, or synthesis. This approach is promising and effective because the two involved transformations (β-pinene epoxidation and epoxide isomerization) can be carried out in a single pot, avoiding several intermediate purification processes, minimizing chemical waste, saving time, and simplifying practical aspects [32].

To our knowledge, as of the current date, there have been no reports found in open literature regarding one-pot reactions for the transformation of β-pinene into myrtanal, myrtenol, or perillyl alcohol as the main products. Few reports exist regarding the one-pot reaction of a similar monoterpene, α-pinene, into campholenic aldehyde primarily.

However, these systems are not highly selective towards the aldehyde; instead, the route is quite competitive, yielding various products. Selectivity towards the aldehyde was increased over the bifunctional PrAlPO-5 catalyst [33] by decreasing the (Al + P)/Pr ratio that enhanced Lewis acidity, reaching up to 90 % at complete conversion (70 °C, 12 h, chloroform as solvent, and air as the oxidizing agent). Zeolite Y encaged Ru (III) and Fe(III) complexes [34], prepared by the flexible ligand method, showed complete conversion of α-pinene towards campholenic aldehyde (35.9 %), α-pinene epoxide (34.1 %), and verbenone (20.7 %) after 18 h at 80 °C, using H_2O_2 as the oxidizing agent and acetonitrile as solvent. V-MCM-41 [35] synthesized via the direct hydrothermal method, exhibited an α-pinene conversion of 12.8 % with selectivities up to 13.4 % for campholenic aldehyde, 15.9 % for 1,2 pinanediol, 36.3 % for trans-sobrerol, and 11.4 % for verbenol (70 °C, 7 h, H_2O_2 as the oxidizing agent, and acetonitrile as solvent). Outdated papers reported Co/SiO_2 [36] and Ti-HMS [37,38] as catalysts that exhibited low α-pinene conversions, typically below 40 %, under the tested reaction conditions.

Although significant progress has been evidenced in the field of one-pot catalytic reactions over the past decades, these reactions have not yet found general application in the production of fine chemicals due to the difficulty of reaction control [39]. Hence, this study aims to utilize the catalysis-in-tandem approach [40], which involves using multiple catalysts combined in a single reaction vessel, undergoing a sequence of precisely staged catalytic steps, specifically monoterpene epoxidation and epoxide rearrangement. This research focus was to investigate the catalytic system composed of MgO, for promoting the β-pinene epoxidation through a Payne system with H_2O_2, and a Lewis acid catalyst based on Me/Support (Me = Sn, Fe, Cu, Co; Support = MCM-41, SBA-15), favoring the rearrangement of β-pinene epoxide, under compatible and mild reaction conditions. The aim was to establish optimal reaction conditions for the selective synthesis of myrtanal from a biomass-derived source like β-pinene.

2. Experimental section

2.1. Materials

Commercial reagents were used as received unless stated otherwise. Reagents for the synthesis of mesoporous catalysts were myristyltrimethylammonium bromide (MTAB, 99 wt%, Sigma Aldrich), tetraethyl orthosilicate (TEOS, 98 wt%, Sigma-Aldrich), ammonium hydroxide (NH_4OH, 29 wt%, Merck), poly(ethylene glycol)-block-poly(propylene glycol)-block-poly(ethylene glycol) (P123, PEG 30 wt%, Sigma-Aldrich, molecular weight of 5800), hydrochloric acid fuming (HCl, 37 wt%, Merck), iron(III) nitrate nonahydrate (Fe(NO_3)_3·9H_2O, 99.5 wt%, PanReac AppliChem), copper(II) nitrate trihydrate (Cu(NO_3)_2·3H_2O, 99.5 wt%, Carlo Erba), cobalt(II) nitrate hexahydrate (Co(NO_3)_2·6H_2O, 100 wt%, J.T. Baker), and stannous chloride dihydrate (SnCl_2·2H_2O, 100 wt%, AlfaAesar). Reagents for catalytic tests were β-pinene (99 wt%, Sigma-Aldrich), hydrogen peroxide (H_2O_2, 30 % w/v, PanReac AppliChem), acetone (99.9 wt%, PanReac AppliChem), acetonitrile (99.5 wt%, Merck), and magnesium oxide (MgO, 99.6 wt%, J.T. Baker). Reagents for the quantification of H_2O_2 were cerium (IV) sulfate solution (Ce(SO_4)_2·4H_2O, 0.1 mol/L, Titripur, Merck), and manganese (IV) oxide (MnO_2, > 99 wt%, Sigma-Aldrich).

2.2. Synthesis of mesoporous supports

MCM-41 and SBA-15 supports were synthesized following the procedures reported by Grün et al. [41] and Shah et al. [42], respectively. In the case of MCM-41, the template MTAB was dissolved in deionized water under magnetic stirring (750 rpm) to achieve a concentration of 0.055 mol L^{-1}. The pH was adjusted with NH_4OH, and TEOS was then added dropwise using a Masterflex model 77200–60 peristaltic pump (0.7 mL min^{-1}). The molar ratio of the mixture was 1 TEOS: 0.1380

Table 2
Description of the prepared catalysts.

Entry	Support	Metal	Nominal loading (% wt.)[a]	Catalyst
1	MCM-41	Sn	2.96	SnM1
2	MCM-41	Sn	5.16	SnM2
3	MCM-41	Fe	5.06	FeM1
4	MCM-41	Cu	5.06	CuM1
5	MCM-41	Co	5.07	CoM1
6	SBA-15	Sn	4.95	SnS1
7	SBA-15	Sn	10.10	SnS2
8	SBA-15	Fe	3.08	FeS1
9	SBA-15	Fe	5.11	FeS2
10	SBA-15	Cu	5.04	CuS1
11	SBA-15	Co	5.27	CoS1

[a] Calculated as the ratio of metal mass to support mass.

MTAB: 1.6280 NH$_4$OH: 147.0995 H$_2$O. The resulting suspension was stirred at room temperature for 1 h, and the precipitate was filtered, dried overnight at 100 °C, and calcined at 550 °C for 5 h at a heating rate of 1 °C min^{-1}. Typical synthesis conditions included 22.43 g MTAB, 101.71 g TEOS, 104.60 mL NH$_4$OH, and 1.2 L of deionized water.

For SBA-15, P123 was dissolved in a mixture of deionized water and HCl (2 M) under magnetic stirring (450 rpm) at room temperature for 1 h. Subsequently, TEOS was slowly added using a peristaltic pump (0.42 mL min^{-1}). The molar ratio of the mixture was 1 TEOS: 0.0058 P123: 5.7757 HCl: 195.9030 H$_2$O. The mixture was stirred at 40 °C and 500 rpm for 24 h, then transferred to a Teflon flask for hydrothermal treatment at 100 °C for 48 h. The precipitated solid was filtered, washed with abundant deionized water, dried for 24 h at room temperature, and finally calcined for 24 h at 550 °C with a heating rate of 1 °C min^{-1}. Typical synthesis conditions included 2.2450 g P123, 4.2687 g TEOS, 60.0182 g HCl (2 M), and 15.0185 g of deionized water. Schemes of the experimental methodology are presented in Figures S1 and S2.

2.3. Synthesis of Metal-Modified catalysts

The anchoring of the metals as the active phases onto supports was conducted through the wetness impregnation procedure (Figure S3). In this method, 40 mL of an aqueous solution of the salt precursor with a specified loading, was added to 1 g of the previously dried support. The resulting mixture was stirred continuously at 750 rpm for 2 h at room temperature and subsequently dried overnight at 80 °C. Then, the synthesized materials (Table 2) were activated by calcination at 550 °C for 5 h at a heating rate of 1 °C min^{-1}.

2.4. Catalyst characterization

The metal-modified mesoporous catalysts were thoroughly analyzed by several techniques. The concentration of the metals (Sn, Fe, Cu, and Co) in the catalysts was determined using inductively coupled plasma optical emission spectroscopy (ICP/OES) with a spectrometer coupled to Plasma iCAP XP (Thermo Scientific). A microwave digestor (Ethos Easy model, Milestone) equipped with 24 positions and an acid purifier (Duopur model, Milestone) was used for sample preparation. Powder X-ray Diffraction patterns (XRD) were obtained using a Malvern-PANalytical Empyrean 2012 diffractometer equipped with a PIXcel3D detector and a copper source (λ = 1.541874 Å). The measurements were conducted at 45 kV and 40 mA, with a low Bragg range of 2θ = 0.5–10°. The goniometer was configured for omega/2theta scans, employing reflection transmission spinner mode with a 4 s rotation period. The scan step size was 0.02°, and each step took 80 s.

The textural properties were investigated by nitrogen physisorption isotherms at 77 K acquired using a Micromeritics ASAP 2020 PLUS instrument. Before analysis, the samples underwent pretreatment at 350 °C for 8 h under a high vacuum for degassing. Surface areas were determined utilizing the BET model, while the pore size distribution was

calculated using the BJH model for the desorption isotherm, incorporating the Harkins and Jura correction [43]. This correction accounts for surface tension and capillary forces influencing nitrogen desorption in small pores. The morphology of the catalysts was examined via transmission electron microscopy (TEM) using a TECNAI F20 Super Twin microscope operating at a resolution of 0.1 nm with an acceleration voltage of 200 kV. The microscope was equipped with a GATAN US 1000XP-P chamber. The samples were dispersed in an ethanol mixture using an ultrasonic bath for 10 min at room temperature and subsequently placed on the Cu lacey carbon grid of 200 mesh and allowed to dry. For determining the elemental composition in the materials, an Oxford Instruments XMAX EDX detector was employed. To calculate the average size of metal particles, the diameter of approximately 250 particles was measured using ImageJ software.

The acidity type of mesoporous catalysts was assessed through infrared spectroscopy using a Frontier FT-IR spectrometer (PerkinElmer, spectrum 65 model) with pyridine (≥ 99 %) as a probe molecule. This method enabled both qualitative and quantitative determination of Brønsted and Lewis acid sites. The spectrometer was equipped with a high-resolution Mercury Cadmium Telluride (MCT) detector and a diffuse reflectance cell (DRIFT). Spectra were recorded with a resolution of 4 cm min^{-1}, ranging from 1750 to 1350 cm^{-1}, over 40 sweeps; the samples were pressed into thin pellets (5–10 mg). Before analysis, the sample underwent pretreatment, gradually reaching 550 °C at a rate of 1 °C min^{-1} and held at that temperature for 5 h. Subsequently, the DRIFT cell's sample holder was heated to 400 °C (10 °C min^{-1}) in a helium flow, capturing spectra at 10 °C intervals (blanks). The pyridine adsorption process was initiated at 40 °C for 30 min, followed by the removal of excess pyridine from the solid surface using a helium flow for 30 min. Desorption started up to 400 °C (10 °C min^{-1}), with spectra recorded every 10 °C. Finally, the difference between the spectra with pyridine and blanks was calculated; Brønsted acid sites (BAS) and Lewis acid sites (LAS) were determined using spectral bands at 1545 cm^{-1} and 1450 cm^{-1}, respectively [44].

The determination of total acidity strength was performed using ammonia-temperature programmed desorption (NH$_3$-TPD) on a Micromeritics Autochem 2920 instrument. Initially, around 100 mg of the sample underwent in-situ activation at 550 °C for 30 min (10 °C min^{-1}). Subsequently, the sample was cooled to 50 °C under helium flow of 50 mL min^{-1} and saturated with a gas mixture containing 0.3 vol% NH$_3$/He (50 mL min^{-1}) for 90 min. The physisorbed NH$_3$ was then flushed with helium (50 mL min^{-1}) at 50 °C for 1 h; lastly, the sample underwent heating to 600 °C (10 °C min^{-1}) under a helium flow of 50 mL min^{-1} for the desorption of NH$_3$. Eq. (1) was used to quantify the acidity strength based on the calibration of the TCD signal and the NH$_3$ concentration, where C$_{Des}$ corresponds to NH$_3$ acidity (mol NH$_3$ g^{-1}), m$_{cat}$ is the mass of the catalyst, $\dot{V}_{He}$ is the volumetric flow of the carrier gas (50 mL He min^{-1}), V$_m$ is the molar volume of one mole of an ideal gas at standard conditions (22.4 L mol^{-1}), β is the heating rate (10 °C min^{-1}), and C$_i$ is the ammonia concentration (% vol).

$$C_{Des} = \frac{1}{m_{cat}} \frac{\dot{V}_{He}}{V_m} \frac{1}{\beta} \int_{T_0}^{T_f} C_i dT \qquad (1)$$

X-ray photoelectron spectroscopy (XPS) analyses were conducted utilizing a Specs X-ray photoelectron spectrometer (NAP-XPS) equipped with a PHOIBOS 150 1D-DLD analyzer. A monochromatic Al-Kα source (1486.7 eV, 13 kV) was employed, and the step energy for general spectra was set at 85.36 eV, while for high-resolution spectra, it was 20 eV. 20 scans were performed for the high-resolution spectra and 5 scans for general spectra. Charge compensation was applied during sample measurements with an energy of 3 eV and 20 μA. All spectra were calibrated using the adventitious carbon 1 s peak at 285.0 eV. A Shirley-type background was subtracted from the spectra, and CasaXPS software was utilized for processing the XPS data.

In our recent work [18], MgO was thoroughly characterized using

Table 3
Metal loading, unit cell parameters, and textual properties of catalysts based on MCM-41 and SBA-15.

Catalyst	% Metal[a]	2θ (°)	d_100[b] (nm)	a_0[c] (nm)	ACS[d] (nm)	BET area (m²/g)	Pore volume (cm³ g⁻¹)	APS[e] (nm)	MC[f] (molec nm⁻²)
MCM-41	0.00	2.76	3.20	3.69	19.29	1394	0.49	2.31	0.00
SnM1	1.25	2.82	3.13	3.61	24.40	1188	0.47	1.66	0.05
SnM2	2.17	2.85	3.10	3.58	22.86	1113	0.42	1.66	0.10
FeM1	8.50	2.87	3.07	3.55	20.24	954	0.26	1.66	0.96
CuM1	5.59	2.98	2.96	3.42	18.04	610	0.25	3.37	0.87
CoM1	4.55	3.01	2.93	3.39	15.96	1803	0.96	3.39	0.26
SBA-15	0.00	0.96	9.19	10.61	62.98	860 [45]	n.r	n.r	0.00
SnS1	2.32	0.88	10.03	11.58	165.89	611	1.23	7.70	0.19
SnS2	2.24	n.a	n.a	n.a	n.a	628	1.22	7.55	0.18
FeS1	5.07	0.93	9.49	10.96	123.98	496	0.96	6.37	1.10
FeS2	5.14	0.91	9.70	11.20	96.22	617	1.09	6.42	0.90
CuS1	4.54	0.91	9.70	11.20	150.81	555	1.08	6.44	0.78
CoS1	5.35	0.90	9.80	11.32	165.89	533	1.17	7.69	1.03

[a] The weight percentage of the metal was determined by ICP/OES.
[b] The interplanar spacing for the plane (1 0 0) (d_100) was calculated using the Bragg equation, Eq. (7).
[c] The unit cell parameter (a_0) was calculated using Eq. (8).
[d] The average crystal size (ACS) was calculated with the Scherrer equation, Eq. (9).
[e] The average pore size (APS) was estimated from the pore size distributions (Fig. 3.C and 3.D).
[f] Metal coverage (MC) = (% metal/100)*(N_A/MW)*(1/BET), where N_A is Avogadro's number and MW is the molecular weight of metal. n.a: Not available because the (1 0 0) Bragg reflection was not observed. n.r: Not reported.

various techniques, including XRD, nitrogen adsorption–desorption isotherms, thermogravimetric analysis (TGA), Fourier transform-infrared spectroscopy (FTIR), and scanning electron microscopy-energy dispersive X-ray spectroscopy (SEM-EDX).

2.5. Catalytic measurements

The one-pot catalytic reactions were performed in 2 mL batch reactors, capped vials covered with silicone septa. The reaction temperature was maintained by immersing the vials in a well-stirred oil bath controlled by an EKT Hei-Con Heidolph controller. Catalytic tests were carried out using a sufficiently high liquid volume-to-catalyst mass ratio and vigorous agitation (1000 rpm) to overcome external mass-transfer limitations. Additionally, small catalyst particles (<75 μm) were utilized to suppress internal mass-transfer limitations. Reactions were stopped by cooling the vials in an ice bath, followed by separating catalysts from the reaction mixture through centrifugation at 3000 rpm for 8 min. Two catalysts were employed in the heterogeneous system, MgO, renowned for its excellent catalytic activity in the epoxidation of monoterpenes [17,18], and acidic mesoporous materials (Table 2) to promote the isomerization of epoxide. In a typical experiment, 0.1 mmol of β-pinene was loaded into the reactor, with weight ratios of 1: 0.72: 1.2: 30.3: 19.7: 15.7: 0.8 for β-pinene: acidic catalyst: MgO: H₂O: acetone: acetonitrile: H₂O₂, the suspension was stirred at 1000 rpm at 50 °C. An aliquot of the centrifuged mixture was utilized for quantifying H₂O₂, while MnO₂ was added to the remaining mixture for oxidant decomposition before GC–MS analysis.

The reaction products were identified using gas chromatography coupled with mass spectrometry, employing a GC–MS Agilent 7890 N equipped with a DB-1 column (30 m, 320 μm, 0.25 μm), a FID detector, and an autosampler. The carrier gas was He (30.462 cm s⁻¹, 2.2912 mL min⁻¹), with a split ratio of 15:1. The detector temperature was set at 250 °C, with an injection volume of 1 μL. The oven temperature was initially kept at 70 °C for 2 min, followed by heating up to 130 °C (10 °C min⁻¹) for 1 min, and finally, an increase to 180 °C (20 °C min⁻¹). The β-pinene conversion ($X_β$), the selectivity (S_j), and the yield to the product j (Y_j) were calculated using Eqs. (2)-(4).

$$X_β(\%) = \frac{C_{β,0} - C_{β,t}}{C_{β,0}} *100 \qquad (2)$$

$$S_j(\%) = \frac{C_{j,t}}{C_{β,0} - C_{β,t}} *100 \qquad (3)$$

$$Y_j(\%) = \frac{C_{j,t}}{C_{β,0}} *100 \qquad (4)$$

$C_{β,0}$, $C_{β,t}$, and $C_{j,t}$ denote the initial molar concentration of β-pinene, the molar concentration of β-pinene after time t, and the molar concentra-
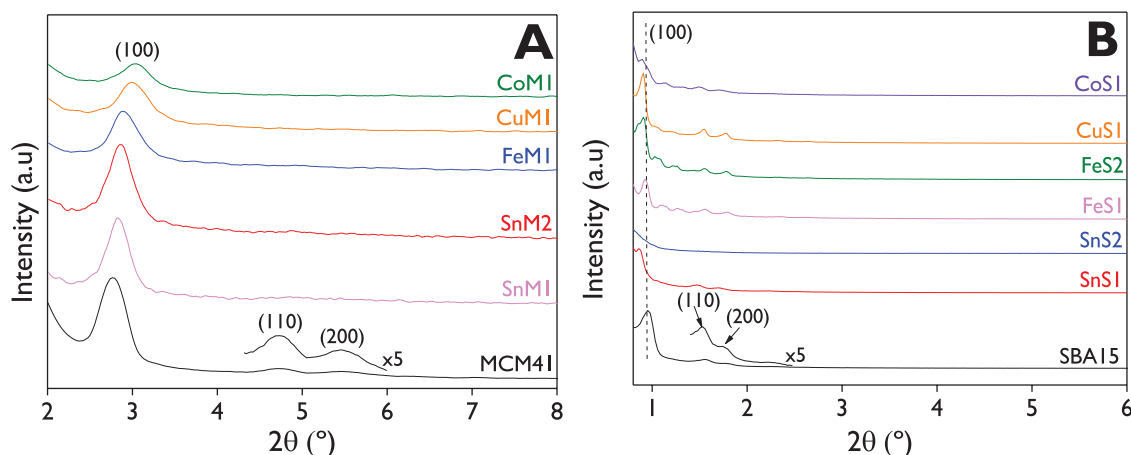

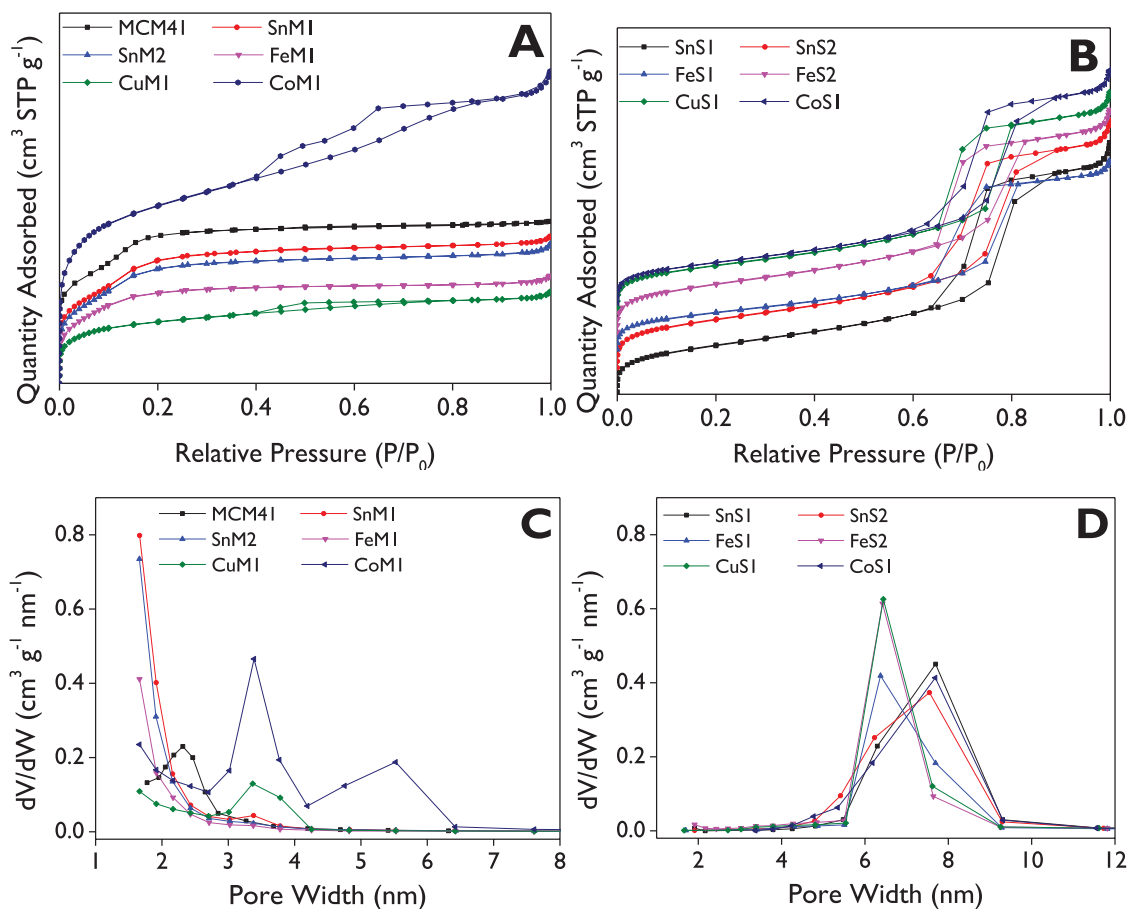**Fig. 2.** XRD patterns of catalysts based on **(A)** MCM-41 and **(B)** SBA-15.

Fig. 3. N_2 adsorption–desorption isotherms **(A, B)** and pore size distributions **(C, D)** for catalysts based on MCM-41 **(A, C)** and SBA-15 **(B, D)**.

tion of the product j after time t in the reaction mixture, respectively; concentrations were calculated with the area normalization method.

2.6. Quantification of oxidizing agent

The H_2O_2 concentration was monitored via cerimetric titration, as reported previously in our work [18]. Briefly, the yellow cerium (IV) sulfate reacts with H_2O_2 to produce colorless cerium (III) sulfate, sulfuric acid, and oxygen. A 100 μL sample was placed into a beaker with 5 mL of deionized water and titrated using a Metrohm 775 Dosimat equipment. The endpoint was reached when the solution changed from colorless to yellow, indicating an excess of titrant agent in the medium. The concentration in wt. % was calculated using Eq. (5), where θ_{SF} is the stoichiometric factor (1/2 for $H_2O_2/Ce(SO_4)_2$), C_T is the concentration of the titrant agent, V_s is the spent volume for the sample titration, V_b is the spent volume of the titrant for the blank test (5 mL of deionized water), $MW_{H_2O_2}$ is the molecular weight of H_2O_2, and W_s is the weight of the sample. The H_2O_2 conversion, as defined in Eq. (6), was calculated using the initial molar concentration ($C_{H_2O_2,0}$).

$$C_{H_2O_2} = \frac{\theta_{SF}C_T(V_T - V_b)MW_{H_2O_2}}{W_s} *100 \qquad (5)$$

$$X_{H_2O_2}(\%) = \frac{C_{H_2O_2,0} - C_{H_2O_2}}{C_{H_2O_2,0}} *100 \qquad (6)$$

3. Results and discussion

3.1. Catalyst characterization

3.1.1. Chemical analysis

The quantification of metals in the catalysts, determined by ICP/OES, is presented in Table 3. Values ranging from 0.0 % (unmodified supports) up to 8.5 wt% (FeM1) were obtained; clearly, these values differ from the nominal metal loadings reported in Table 2.

3.1.2. X-ray diffraction

Fig. 2 presents the XRD patterns for the prepared catalysts based on MCM-41 (Fig. 2.A) and SBA-15 supports (Fig. 2.B). Three diffraction peaks corresponding to reflections (100), (110), and (200) are observed in all the catalysts, which are characteristic of the typical hexagonal arrangement of these two materials [6,46–49]. The main diffraction peaks for the MCM-41 series of catalysts are located at 2θ = 2.8°, 4.8°, and 5.4°, corresponding to the crystallographic planes (100), (110), and (200), respectively. It is noteworthy that in all materials, the main peak associated with the (100) crystallographic plane can be clearly observed, but in the metal-modified MCM-41 catalysts, the intensity of the other two peaks decreased compared to the support. Furthermore, slight shifts (Δ2θ) were observed in the (100) peak in the catalysts after the impregnation of metals, with a maximum shift of 0.25° for CoM1. Additionally, XRD of the materials that contained Co, Cu, or Fe indicates a decrease in the well arrangement of the hexagonal pores due to a decrease in the intensity of the main diffraction peak, while materials with Sn exhibit an XRD like the support.

For the SBA-15 series of catalysts, the same three crystallographic planes are located at 2θ = 1.0°, 1.6°, and 1.8°, respectively. Notably, the
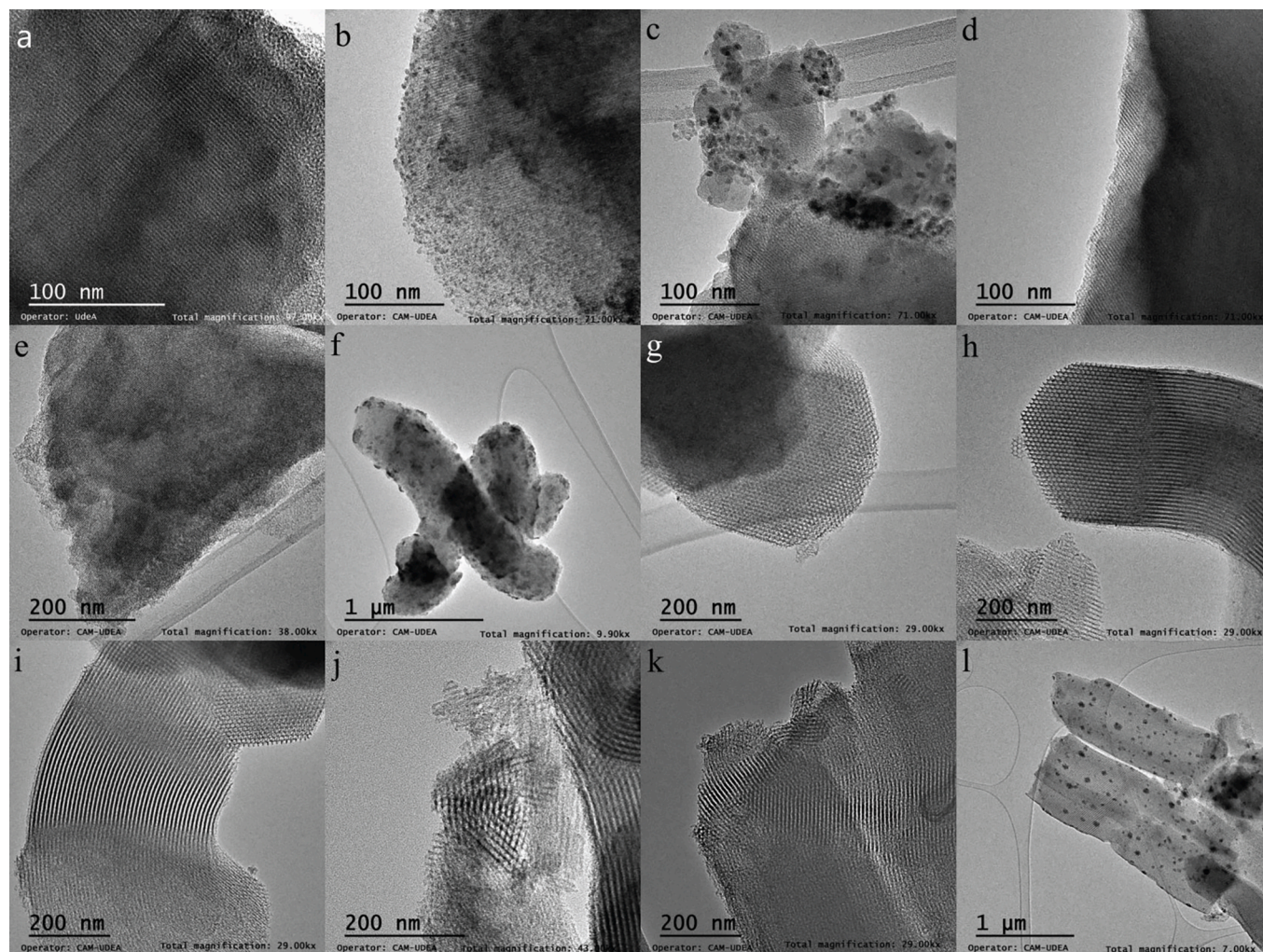
Fig. 4. Transmission Electron Microscopy (TEM) images of **a.** MCM-41, **b.** SnM1, **c.** SnM2, **d.** FeM1, **e.** CuM1, **f.** CoM1, **g.** SnS1, **h.** SnS2, **i.** FeS1, **j.** FeS2, **k.** CuS1, **l.** CoS1.

intensity of SnS2 significantly decreased in comparison with the SBA-15 support and the other metal-modified catalysts. This decrease can be attributed to the high Sn loading. Similar results regarding the high loading of Fe anchored on SBA-15 have been reported, where the intensity of the (1 0 0) plane almost completely disappeared [45]. On the other hand, the catalyst with Co (CoS1) exhibited an appreciable loss of hexagonal rearrangement, as suggested by the low intensity of the main diffraction peak. Co-supported on MCM-41 (CoM1) also showed the lowest crystallinity due to a broad peak and low intensity.

The indexing of the diffraction peaks [50,51] can be performed using Bragg's law, Eq. (7), and the interplanar spacing (d) for the hexagonal structure can be calculated with Eq. (8), where d represents the interplanar spacing for the plane (h k l), with h, k, and l being the Miller indices. θ denotes the diffraction angle, λ is the wavelength of the incident X-ray beam (0.154 nm for a copper lamp), and a_0 is the unit cell parameter in the hexagonal structure.

$$n\lambda = 2d\sin(\theta) \tag{7}$$

$$a_0 = \frac{2d}{\sqrt{3}}\sqrt{h^2 + hk + k^2} \tag{8}$$

Additionally, the average crystal size (ACS) can be calculated using the Scherrer equation [52], described by Eq. (9), where K is the shape factor constant (0.94), and β (in radians) is the full width at half maximum (FWHM) of the most intense diffraction peak (1 0 0).

$$ACS = \frac{K\lambda}{\beta\cos(\theta)} \tag{9}$$

The results of the unit cell parameters (d_{100} and a_0) and the ACS are presented in Table 3. The values of d_{100} and a_0 for the metal-modified MCM-41 catalysts decreased compared to the MCM-41 support, as expected from the shift in the diffraction peak associated with the (1 0 0) plane. In contrast, for the catalysts based on SBA-15, these values increased with respect to the SBA-15 support, which is evidenced with a shift to the left of the main diffraction peak. It is noteworthy that the corresponding values of d_{100} and a_0 for catalysts based on SBA-15 are around three times those for catalysts based on MCM-41. Additionally, the loading of Sn onto MCM-41 (SnM1 and SnM2) and Fe onto SBA-15 (FeS1 and FeS2) seems to have no significant influence on d_{100} and a_0.

Among the MCM-41 catalysts, SnM1 and SnM2 exhibited the highest ACS values (24.4 and 22.9 nm, respectively) showing a narrower main diffraction peak at the lowest Bragg angle (Eq. (9) and Fig. 2.A). Conversely, the lowest ACS value (16.0 nm) was obtained for CoM1, based on its wider peak and the most rightward shift ($2\theta = 3.01°$). For the SBA-15 catalysts, all materials exhibited values of at least 63 nm; SnS1 showed the highest value (165.9 nm).

3.1.3. Textural properties

The N_2 adsorption–desorption isotherms (Fig. 3.A and B) of the catalysts were measured to determine the textural properties, such as the
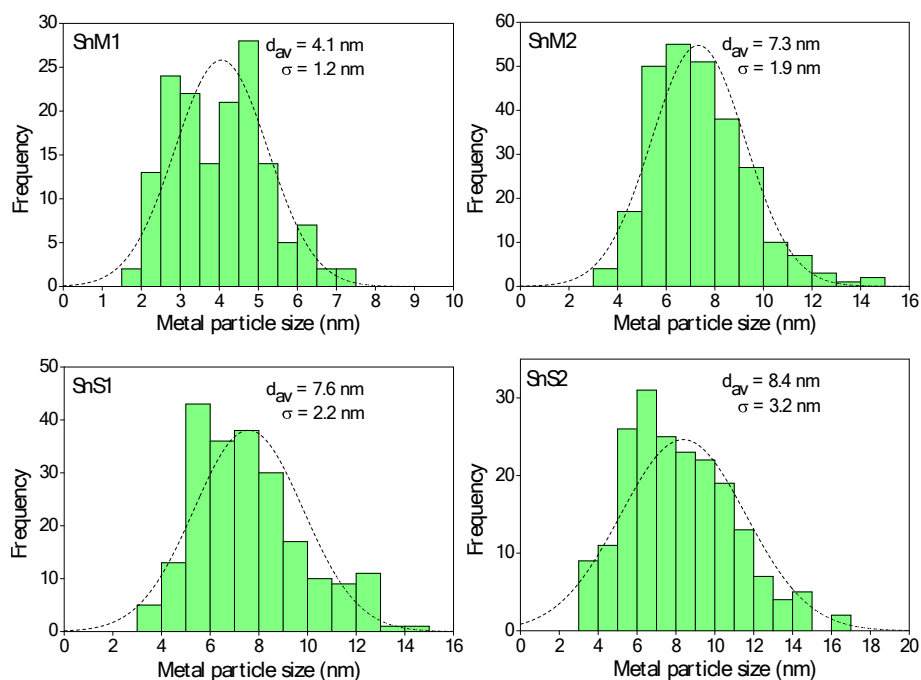
Fig. 5. Tin size distribution of tin-modified catalysts.

BET surface area, pore volume, and average pore size (APS), as illustrated in Table 3. The presence of mesopores in catalysts based on MCM-41 and SBA-15 is confirmed by Fig. 3.A and B, respectively. All materials exhibit type IV-like isotherms according to the IUPAC classification [53–55]. However, notice that the MCM-41 support and the catalysts based on MCM-41, such as SnM1, SnM2, and FeM1, did not exhibit the hysteresis loop, which can be attributed to the low pore sizes of those materials (Table 3), practically at the boundary of micropores and mesopores, as has been previously reported [48,56]. All materials in Fig. 3.A show strong adsorption at around a relative pressure of 0.2. Contrarily, isotherms of all materials based on SBA-15 (Fig. 3.B) exhibited a typical hysteresis loop of type H1 with steep condensation and evaporation branches between relative pressures of 0.7 and 0.75, indicating a narrow mesopore size distribution and demonstrating the good quality of the materials [57]. In addition, the further increase in the adsorbed volume at the end of the isotherm can be associated with the adsorption on the external surface of the porous materials [57]. The isotherms for SBA-15 materials allow the conclusion that they belong to porous systems that consist of cylindrical geometry pores opened on both sides [58].

The BET areas (Table 3) of the catalysts based on MCM-41 show that the support exhibited a very high BET area (1394 $m^2 g^{-1}$) and this value decreased along with the incorporation of different metals like Sn, Fe, and Cu, obtaining a value below 50 % for CuM1 (610 $m^2 g^{-1}$), suggesting possible pore blocking or clogging in those materials. For catalysts based on SBA-15, the surface area of the support is 860 $m^2 g^{-1}$ [45]. When the metals were anchored onto the support by wetness impregnation, like catalysts with MCM-41, a decrease in the surface areas was observed, reaching the lowest value for the FeS1 catalyst (496 $m^2 g^{-1}$) signifying a loss of about 42 % of the area concerning the support. In this way, it is clear that the incorporation of metals significantly affects the catalyst surface, reducing their BET area, as reported in similar catalysts for Prins condensation and isomerization reactions [45,48]. On the other hand, the Sn loading did not exhibit an effect on the BET area for MCM-41 and SBA-15 catalysts, while appreciable differences were observed with different Fe loadings onto SBA-15. The BET surface area was utilized in conjunction with the metal percentage determined by ICP-OES to determine the metal coverage (MC), as reported in Table 3. This parameter represents the number of metal entities per unit area of

the catalyst.

Furthermore, notice that the pore volume (Table 3) can be directly related to the BET area, reaching the highest values for the MCM-41 support (0.49 $cm^3 g^{-1}$) and SnS1 (1.23 $cm^3 g^{-1}$), among each series of catalysts. However, although the BET areas for catalysts based on MCM-41 were larger than those for SBA-15 materials, the pore diameter and the pore volume of SBA-15 catalysts are much larger than for MCM-41 catalysts [59], which can be attributed to the cylindrical shape of the pores in the SBA-15 which allows low packing density, existing more space between the pores, resulting in a larger total pore volume. These characteristics are useful for the fabrication of electrochemical sensors [60] and dental applications [61].

The pore size distributions for catalysts based on MCM-41 and SBA-15 are presented in Fig. 3.C and D, respectively. Fig. 3.C shows that the average pore size (APS) for the materials MCM-41, SnM1, SnM2, and FeM1 is very close to 2 nm, limiting between micropores and mesopores, while distributions for CuM1 and CoM1 are shifted to the right, with APS values of 3.37 and 3.39 nm, respectively. This observation aligns with the behavior of the N_2 isotherms. For SBA-15 catalysts (Fig. 3.D), SnS1, SnS2, and CoS1 exhibit closer values between 7.55 and 7.70 nm, while FeS1, FeS2, and CuS1 show lower values between 6.37 and 6.44 nm. Therefore, it can be concluded that the loading of Sn and Fe onto the mesoporous supports did not significantly affect the pore size of the catalysts.

3.1.4. TEM-EDX analysis

The TEM images for the prepared catalysts are shown in Fig. 4 and Figs. S4-S15. Fig. 4.a–f and Figs. S4-S9 depict the morphology of the catalysts based on MCM-41, where the characteristic channels with a typical ordered hexagonal array mesostructure for these materials are observed in most of them [48,62]. However, Fig. 4.f and Figs. S9 show the morphology for cobalt-modified MCM-41 (CoM1), which does not clearly exhibit the ordered structure. This aligns with the previous results of XRD (Fig. 2.A), which showed a low intensity of the main diffraction peak, which suggested the absence of a well-arranged structure in that material. Conversely, Fig. 4.a and Fig. S4 show a very high and uniform distribution of hexagonal rearrangement of pores in the unmodified support (MCM-41), validating the successful synthesis of the support. For catalysts based on SBA-15, the TEM images are shown

Table 4
Elemental composition of the prepared catalysts using TEM-EDX analysis.

Catalyst	Weight %		
	Si	O	Metal
SnM1	39.50	46.59	13.91
SnM2	42.99	51.50	5.51
FeM1	45.94	49.94	4.12
CuM1	45.78	51.45	2.77
CoM1	47.25	52.33	0.42
SnS1	47.21	51.02	1.77
SnS2	54.07	40.93	5.00
FeS1	46.96	52.36	0.68
FeS2	47.81	51.31	0.88
CuS1	53.37	44.09	2.54
CoS1	47.58	50.38	2.04

Table 5
Acidic properties of the catalysts by pyridine-FTIR.

Catalyst	Acidity[a] (μmol g^{-1})				Acid sites density[b] (μmol m^{-2})
	Weak	Medium	Strong	Total	
SnM1	11	14	5	30	0.025
SnM2	68	8	5	81	0.073
FeM1	87	5	3	95	0.100
CuM1	81	15	7	103	0.169
CoM1	27	1	8	36	0.020
SnS1	101	24	13	138	0.226
SnS2	93	8	5	106	0.169
FeS1	113	13	12	138	0.278
FeS2	83	11	7	101	0.164
CuS1	102	7	4	113	0.204
CoS1	99	6	9	114	0.214

[a] Measurements at 100 °C: weak + medium + strong; measurements at 200 °C: medium + strong; measurements at 300 °C: strong.
[b] Calculated as total acidity/ BET area.

in Fig. 4.g–l and Figs. S10-S15, revealing excellent ordering in the channels with well-defined and uniform pores, typical of SBA-15 materials [63,64].

The materials modified with Sn in either MCM-41 (Fig. 4.b–c and Fig. S5-S6) and SBA-15 (Fig. 4.g–h and Figs. S10-S11) exhibit well-dispersed metal particles over the supports, as has been detected for Sn nanoparticles in heterogenous catalysts based on microporous and hierarchical zeolite Y-based catalysts [65,66]. The images of mesoporous catalysts with Fe (Fig. 4.d, i, j and Figs. S7, S12, S13) and Cu (Fig. 4.e, k and Figs. S8, S14) suggest that metal nanoparticles are located inside the channels. These results differ significantly from those previously reported for different loadings of Fe and Cu supported onto MCM-41 and SBA-15 [45], where the authors observed Cu nanoparticles in the TEM images of all materials and also Fe nanoparticles in some of the synthesized materials. These notable differences are attributed to the post-grafting procedure utilized by them, which used incipient wetness impregnation with the same salt precursors with a defined volume of salt precursor depending on the support (5.4 mL g^{-1} MCM-41 and 3.0 mL g^{-1} SBA-15), while in this study, wetness impregnation was used, characterized by an excess of the salt precursor solution, which is a more reproducible method and easier to scale-up for the synthesis of a bigger batch of catalysts. Therefore, it is concluded that the post-impregnation procedure in the preparation of the catalysts for the metal nanoparticles is of great importance and influences the location of the active phase in the mesoporous supports.

The elemental maps of silicon, oxygen, and the corresponding metal (Sn, Fe, Cu, Co) for four catalysts, namely FeM1, SnS1, CuS1, and CoS1, are presented in Figures S16-S19. These maps indicate the excellent distribution of metals in the support achieved through wetness impregnation. This conclusion is drawn from the similarity in the physical form of the elemental maps for the metals to the elemental maps of oxygen and silicon in each mesoporous catalyst. Additionally, there is no presence of concentrated or agglomerated regions, further supporting the effective distribution of metals throughout the catalysts.

As previously mentioned for the four Sn-modified catalysts, and despite the qualitative information concluded from the TEM images, the distribution of Sn particle sizes can be obtained from at least 250 measurements from the TEM micrographs for each catalyst, as shown in Fig. 5. The two catalysts based on MCM-41, SnM1 and SnM2, exhibited a lower average particle size with values of 4.1 and 7.3 nm, respectively, in comparison with values for the SBA-15 catalysts, SnS1 and SnS2, with values of 7.6 and 8.4 nm, respectively. Notice that values for materials based on MCM-41 differ significantly, which can be associated with the notable difference in Sn loadings (Table 3). In contrast, no appreciable difference in loading was observed in materials based on SBA-15. The average particle size for several catalysts based on Sn and K-Sn dealuminated zeolite Y was reported [66], showing values ranging from 4.9 nm to 6.1 nm, using SnCl$_4$·5H$_2$O as the salt precursor, and different materials Sn-zeolite Y (SiO$_2$/Al$_2$O$_3$ molar ratio = 5.1, 30, and 80, and the corresponding dealuminated zeolites) using SnCl$_4$·5H$_2$O and SnCl$_2$ as

salt precursors [65], which exhibited average values between 7.3 and 10.4 mm. Interestingly, higher average particle size was observed with higher metal loading in the catalysts in those studies, similar to our findings.

The elemental composition of the catalysts was determined using EDX, and the results are presented in Table 4 as atomic weight percentages. All materials exhibit the presence of Si, O, and the respective metal, with no detectable impurities (weight balance totaling 100 %). The differences in the weight percentages of metals, as compared to the values determined by ICP/OES (Table 3), can be readily explained. EDX in TEM micrographs provides point analysis, meaning that the composition depends on the specific region where the analysis was conducted. On the other hand, ICP/OES is a more robust technique for quantification across the entire sample.

3.1.5. Catalyst acidity

The quantification through adsorption–desorption FTIR analysis of pyridine as a probe molecule for the prepared catalysts is presented in Table 5 and Figure S20. This analysis plays a crucial role in identifying the strength of acid sites (weak, medium, and strong), as well as the type of acidity (Brønsted and Lewis), which needs to be performed at various temperatures (100 °C, 200 °C, and 300 °C). Typical FTIR spectra for the materials are depicted in Figure S20, where the band around 1545 cm^{-1} associated with Brønsted acidity was not observed [65,66]. On the contrary, a well-defined band associated with Lewis acidity was observed around 1450 cm^{-1} in all materials [45,48]. The very slight band around 1480–1490 cm^{-1} has been associated with the presence of Bronsted + Lewis sites [67], indicating only Lewis acid sites for these materials. The intense band around 1595 cm^{-1} corresponds to the interaction of pyridine with hydrogen linked to silanol groups [68]. Therefore, the reported values in Table 5 for the prepared catalysts correspond entirely to the Lewis acidity type. This aligns with previous reports based on Fe, Cu, and Sn-supported mesoporous materials [45,48,63,69,70].

All FTIR spectra of materials show appreciable absorbance changes, decreasing as the temperature increases, indicating no very significant strong acidity in the mesoporous catalysts, as evidenced by the values presented in Table 5. CoM1 exhibited the highest % of strong acidity with a value of 22.2 %, followed by SnM1 with 16.7 %; the other catalysts presented strong acidity < 10 %. On the contrary, FeM1 presented the highest % of weak acidity (91.6 %) followed by CuS1 (90.3 %). SnM1 exhibited the lowest % of weak acidity (36.7 %) and the highest % of medium acidity (46.7 %). SnS1 and FeS1 exhibited the highest total acidity with values of ca. 138 µmol/g. It is noteworthy that total acidity increases with the metal loading, as observed for SnM1 and SnM2 with values of 30 and 81 µmol/g corresponding to Sn loadings of 1.25 and 2.17 % (Table 3), respectively. In contrast, the pairs SnS1 and SnS2, and
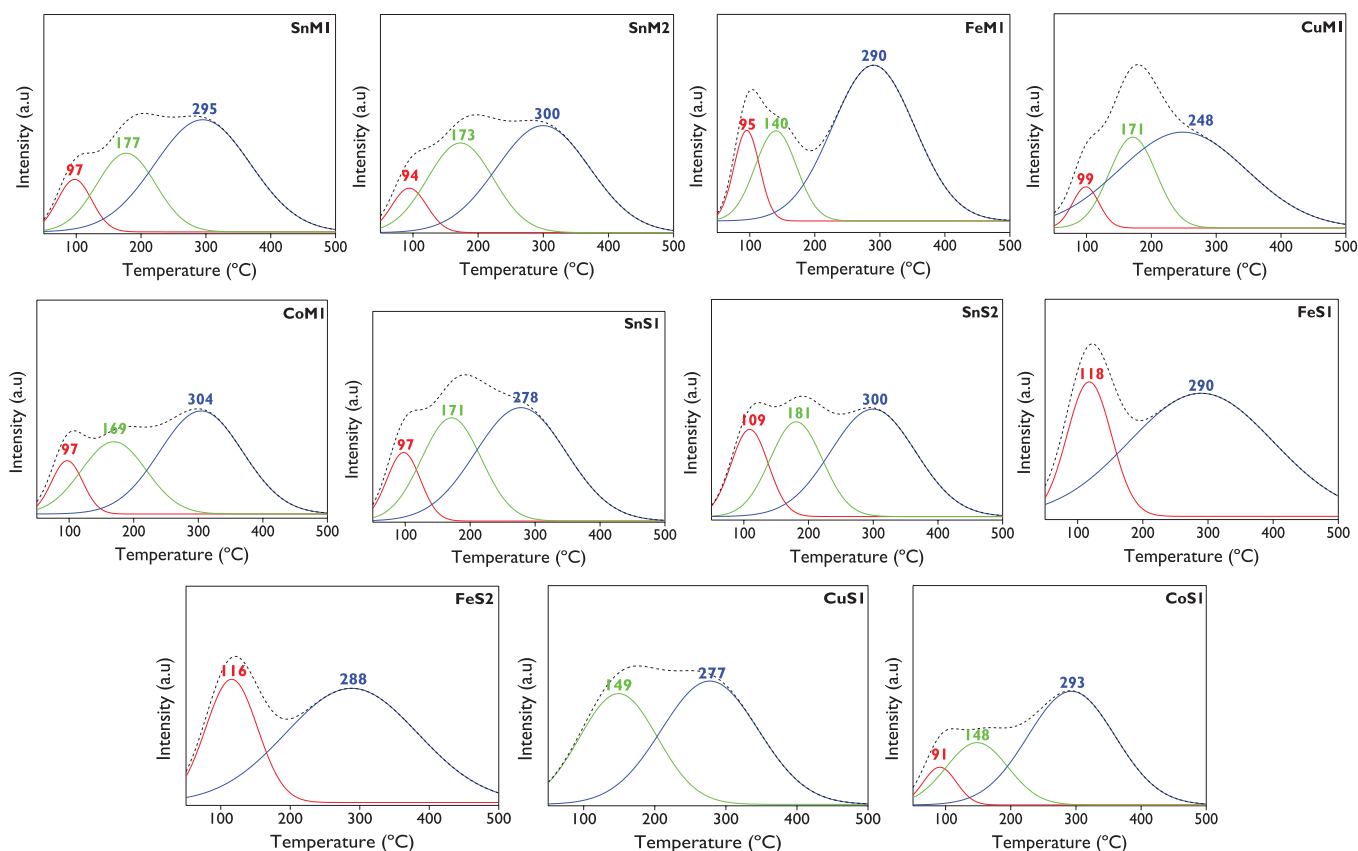
Fig. 6. NH$_3$-TPD profiles for the metal-modified catalysts.

FeS1 and FeS2 differ in the values of total acidity, although these materials have similar metal loadings, as evidenced in Table 3. These differences in the distribution of acid site strengths can be explained by the silanol group environments, as it is well-known that the acidity of mesoporous materials such as MCM-41 and SBA-15 is caused by the silanol groups on the structure [71,72]. Furthermore, Table 5 shows the density of acid sites for each metal-modified catalyst.

The strength of acidity in the catalysts was also investigated using NH$_3$-TPD, which can be classified according to the deconvoluted signals as very weak, weak, medium, and strong acidity with a maximum band in the range < 150 °C, < 250 °C, < 330 °C, and 330–500 °C [48,73], respectively. Fig. 6 shows that none of the materials exhibit deconvoluted signals above 330 °C, associated with strong acidity, verifying the low values previously reported using pyridine-FTIR analysis. Table S1 displays the quantification through NH$_3$ as a probe molecule for all the catalysts.

3.1.6. Surface chemistry

The investigation into the oxidation states on catalytic surfaces and surface chemical composition was conducted using X-ray photoelectron spectroscopy (XPS), employing survey scans in wide scan and high-resolution spectra modes for all metal-modified catalysts based on MCM-41 and SBA-15 supports. The wide spectra for catalysts with Sn, Fe, Cu, and Co are presented in Figures S21-S24, respectively. All materials exhibited characteristic peaks at around 26, 104, 155, 285, 533, and 977 eV binding energy, corresponding to O2s, Si2p, Si2S, C1s, O1s, and oxygen KLL Auger transition, respectively [48,74]. Peaks associated with Sn3d$_{5/2}$ and Sn3d$_{3/2}$ were observed in Figure S21 at around 487 and 496 eV [48], respectively; while peaks linked to Co2p$_{3/2}$ and Co2p$_{1/2}$ were evident in Figure S24 at approximately 780.8 and 795.9 eV [75], respectively. In contrast, peaks associated with Fe (Figure S22) and Cu (Figure S23) were not discernible in the wide XPS spectra. However,

Fig. 7 displays high-resolution XPS spectra for Sn3d, Fe2p, Cu2p, and Co2p for all the catalysts. Additionally, Figure S25 depicts high-resolution spectra of all catalysts for Si2p, showing a peak around 104 eV attributed to Si-O-Si of the silica network, while Figure S26 exhibits O1s spectra with two deconvoluted signals around 533 and 534 eV, attributed to oxygen from the silica framework and silanol groups on the surface, respectively [48].

The Sn3d spectra (Fig. 7) exhibit well-defined spin–orbit doublet peaks at around 487.6 eV and 496.1 eV, associated with Sn^{4+} 3d$_{5/2}$ and Sn^{4+} 3d$_{3/2}$, respectively [63,76], with a separation of ca. ΔV=8.4–8.5 eV [77,78]. In the Fe-supported MCM-41 catalyst (FeM1), peaks at around 710.4 eV and 725.8 eV binding energies correspond to Fe 2p$_{3/2}$ and Fe 2p$_{1/2}$, respectively, indicating the Fe^{3+} oxidation state [77,79]. However, the presence of Fe^{2+} can be inferred after deconvolution of the Fe 2p3/2 signal to a lesser extent compared to Fe^{3+}, as reported in the literature [80]. Fe-supported SBA-15 catalysts (FeS1 and FeS2) did not exhibit clear signals, suggesting the absence of Fe species on the catalyst surface, as indicated by morphology analysis (Fig. 4) that showed their presence within the channels.

Catalysts impregnated with Cu showed clear signals for both Cu 2p$_{3/2}$ and 2p$_{1/2}$ at around 934 eV and 953.7 eV, respectively [77,80,81]. The low-energy peaks of Cu 2p$_{3/2}$ (933.8 eV) are typically attributed to Cu^{2+} in octahedral sites, while high-energy peaks (936.5 eV) correlate with Cu^{2+} in tetrahedral sites [82]. However, the binding energy for Cu$^+$ is quite similar ($\approx$ 933 eV). Therefore, the absence of a strong Cu^{2+} satellite peak around 943 eV led to the conclusion of the presence of only Cu^{1+} species on the catalyst surface (CuS1). Notably, no signals were observed for CuM1, similarly to FeS1 and FeS2 [77,80,82].

XPS spectra for catalysts containing Co displayed spin–orbit components Co 2p$_{3/2}$ and Co 2p$_{1/2}$ at around 780.1 and 795.4 eV [75,83], respectively. The doublet of 2p$_{3/2}$ can be deconvoluted into two peaks at around 780.7 and 782.1 eV, attributed to Co^{3+} and Co^{2+} species,
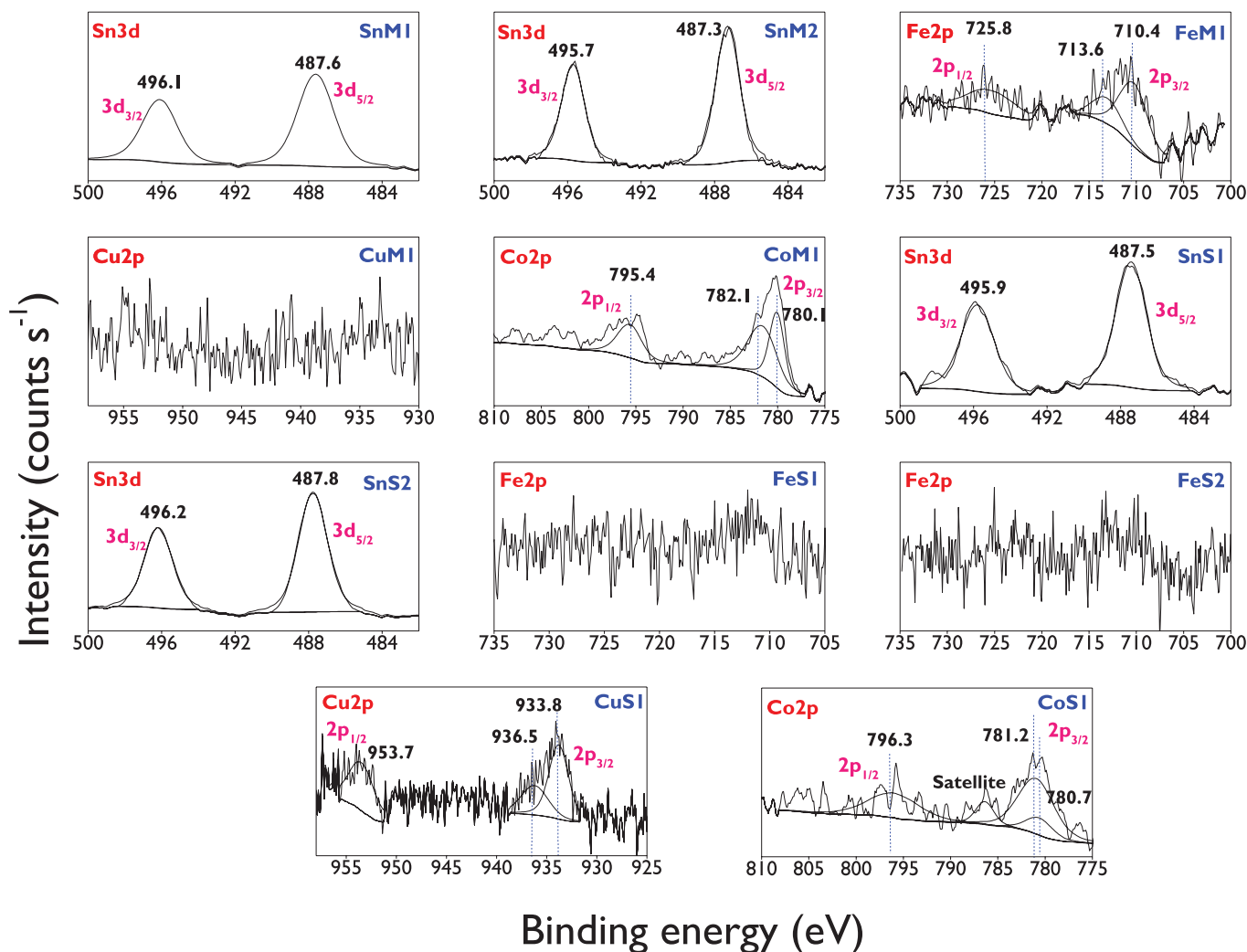
Fig. 7. High-resolution XPS spectra of Sn, Fe, Cu, and Co over MCM-41 and SBA-15.

Table 6
Surface composition of all catalysts.

Catalyst	Weight %							
	O	Si	Sn^{4+}	Fe^{3+}	Fe^{2+}	Cu^{1+}	Co^{3+}	Co^{2+}
SnM1	62.32	36.41	1.28	0.00	0.00	0.00	0.00	0.00
SnM2	61.66	37.11	1.22	0.00	0.00	0.00	0.00	0.00
FeM1	61.30	38.32	0.00	0.27	0.11	0.00	0.00	0.00
CuM1	64.77	35.23	0.00	0.00	0.00	0.00*	0.00	0.00
CoM1	62.03	37.00	0.00	0.00	0.00	0.00	0.42	0.55
SnS1	62.15	37.56	0.29	0.00	0.00	0.00	0.00	0.00
SnS2	62.37	36.62	1.02	0.00	0.00	0.00	0.00	0.00
FeS1	62.23	37.77	0.00	0.00*	0.00*	0.00	0.00	0.00
FeS2	61.94	38.06	0.00	0.00*	0.00*	0.00	0.00	0.00
CuS1	61.91	37.89	0.00	0.00	0.00	0.20	0.00	0.00
CoS1	63.20	36.55	0.00	0.00	0.00	0.00	0.05	0.20

The quantification was performed using the equation $C_x = \frac{I_x/S_x}{\sum I_i/S_i}$, where I_x represents the area of the relative peak of the photoelectrons of element x, and S_x denotes the relative sensitivity factor (RSF) [78], as reported by Scofield [84]: RSF (O1s) = 2.93, RSF(Si2p) = 0.817, RSF(Sn3d$_{5/2}$) = 14.8, RSF(Fe2p$_{3/2}$) = 10.82, RSF(Cu2p$_{3/2}$) = 16.73, and RSF(Co2p$_{3/2}$) = 12.62.
* These values were taken as 0 due to the absence of defined signals in Fig. 7.

respectively. Furthermore, the presence of a satellite peak in the vicinity of the 2p$_{3/2}$ region around 788 eV further demonstrates the existence of cobalt oxides [75].

The surface composition of the catalysts is presented in Table 6. All materials exhibited oxygen content ranging from 61.30 to 64.77 wt%

and silicon content ranging from 35.23 to 38.32 wt%, resulting in O/Si ratios between 1.60 and 1.84. These values are consistent with those previously reported for catalysts based on ordered silica materials [48]. SnM1 showed the highest metal species composition, with 1.28 wt% Sn^{4+}. It is noteworthy that this surface composition of metal species is
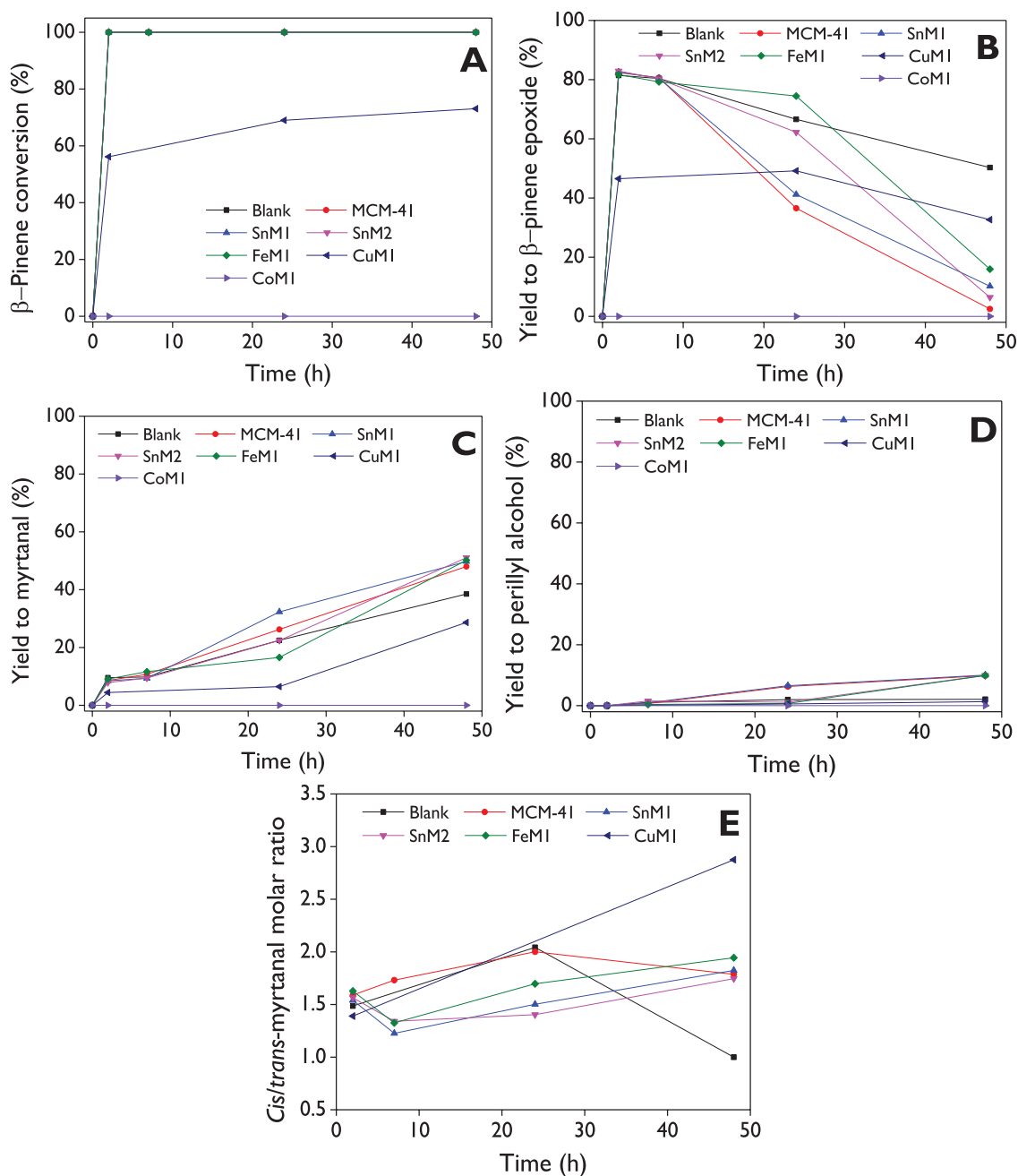
Fig. 8. Role of acidic catalysts based on MCM-41 support in the one-pot transformation of β-pinene: **(A)** β-Pinene conversion, **(B)** yield of β-pinene epoxide, **(C)** yield of myrtanal, **(D)** yield of perillyl alcohol, **(E)** *cis/trans*-myrtanal molar ratio. **Reaction conditions:** 0.1 mmol of β-pinene with weight ratios of 1: 0.72: 1.2: 30.3: 19.7: 15.7: 0.8 for β-pinene: acidic catalyst: MgO: H_2O: acetone: acetonitrile: H_2O_2, 50 °C, 1000 rpm.

notably lower than the elemental composition previously reported by TEM-EDX (Table 4), suggesting that active species are also present within the channels, as it was shown by the TEM images and the lack of defined signals in the high-resolution XPS spectra for some catalysts based on Fe and Cu.

3.2. Catalytic performance

3.2.1. General aspects

Fig. 1 depicts the general scheme of the products obtained in the rearrangement of β-pinene epoxide, including *cis*-myrtanal, *trans*-myrtanal, myrtenol, and perillyl alcohol. However, additional products are yielded in this contribution, with their retention times and mass spectra outlined in section 7 of the Supporting Information. Suggestions for the

corresponding compounds of some of these products are also provided. Additionally, the repeatability of the experiments was investigated using the FeS1 catalyst as presented in Figure S40. Results demonstrated the reliability of the experimental setup.

3.2.2. Conversion and product distribution: Role of the acidic catalyst

The role of the acidic catalyst (Figs. 8-9) was evaluated in the conversion and product distribution in the one-pot tandem transformation of β-pinene with H_2O_2. The first step consists of synthesizing β-pinene epoxide through a Payne system with MgO as a catalyst, achieving complete conversion after 2 h under the tested reaction conditions [17]. The second step corresponds to rearranging the epoxide towards target products like myrtanal (*cis* + *trans*) as the major product, which is greatly influenced by the type of acidic catalyst, as will be evaluated
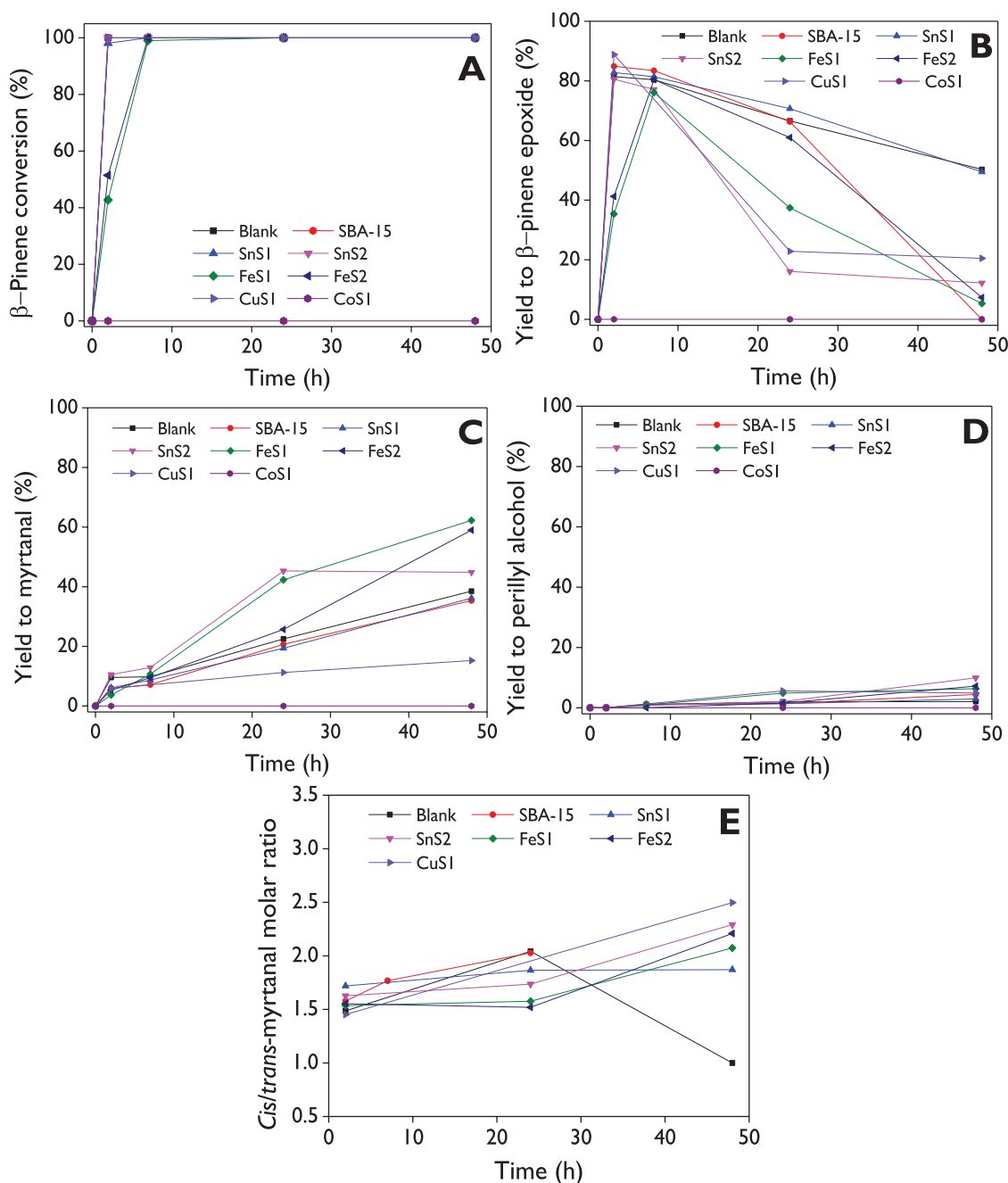
Fig. 9. Role of acidic catalysts based on SBA-15 support in the one-pot transformation of β-pinene: **(A)** β-Pinene conversion, **(B)** yield of β-pinene epoxide, **(C)** yield of myrtanal, **(D)** yield of perillyl alcohol, **(E)** *cis/trans*-myrtanal molar ratio. **Reaction conditions:** 0.1 mmol of β-pinene with weight ratios of 1: 0.72: 1.2: 30.3: 19.7: 15.7: 0.8 for β-pinene: acidic catalyst: MgO: H_2O: acetone: acetonitrile: H_2O_2, 50 °C, 1000 rpm.

below.

The effect of the prepared catalysts on the β-pinene conversion and yield of products based on MCM-41 is illustrated in Fig. 8, while the results with catalysts based on SBA-15 are displayed in Fig. 9. The blank test (without acidic material, Fig. 8.A and 9.A) resulted in complete conversion after 2 h of reaction, as reported for β-pinene [17] and limonene [18] under similar reaction conditions in a Payne system. Additionally, those studies demonstrated that the catalytic epoxidation of both monoterpenes did not proceed in the absence of MgO because it is a heterogeneous reaction. With the MCM-41 support and some metal-modified catalysts such as SnM1, SnM2, and FeM1 (Fig. 8.A), complete conversion can also be reached after 2 h, demonstrating no existence of an antagonistic effect of the acidic material in the first step of the

epoxidation of the substrate. Conversely, the catalyst modified with Cu exhibited a maximum conversion of ca. 73 % after 48 h, while null activity was reached with CoM1. In the case of catalysts based on SBA-15 (Fig. 9.A), complete conversion was reached after 2 h with the support, and the Sn- and Cu-modified materials, while catalysts modified with Fe exhibited conversion values between 42 and 51 % at the same time. However, with these two catalysts, the complete conversion was reached later. Similarly, the CoS1 catalyst exhibited no reactivity of β-pinene in the epoxidation route as CoM1.

The decrease in β-pinene conversion at 2 h with some metal-modified catalysts (CuM1, FeS1, FeS2, CoM1, and CoS1) could suggest blocking of the active sites of MgO caused by the metallic agglomerates, resulting in inhibition of the formation of β-pinene epoxide. However, it can also be
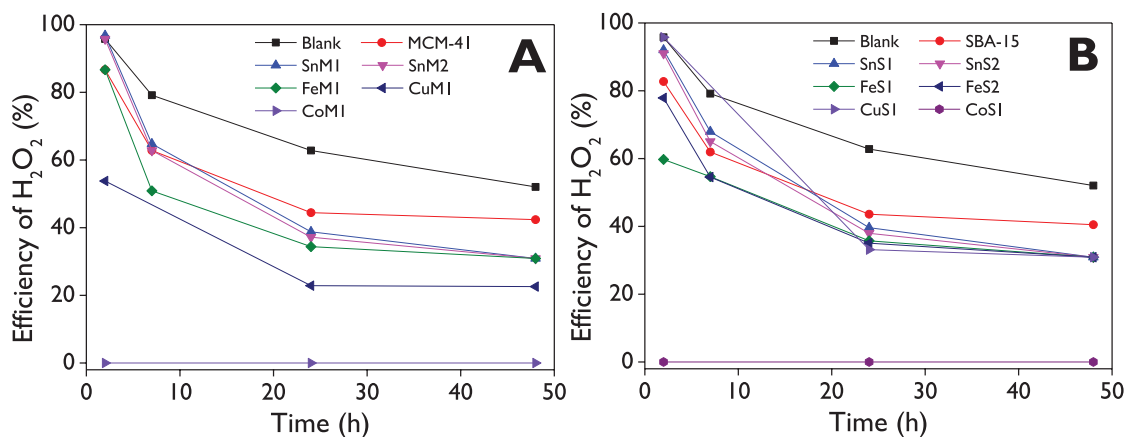
Fig. 10. Efficiency of H_2O_2 in the one-pot transformation of β-pinene with the catalysts based on MCM-41 (A) and SBA-15 (B). Reaction conditions: 0.1 mmol of β-pinene with weight ratios of 1: 0.72: 1.2: 30.3: 19.7: 15.7: 0.8 for β-pinene: acidic catalyst: MgO: H_2O: acetone: acetonitrile: H_2O_2, 50 °C, 1000 rpm. Efficiency was calculated as $X_{H2O2,epox}/X_{H2O2,global}$ [66], where the numerator represents the partial conversion of H_2O_2 through the epoxidation reaction, and the denominator represents the overall conversion of H_2O_2 determined by cerimetric titration.

explained by the rapid consumption of H_2O_2 through decomposition caused by metals, as reported previously in the literature [85,86], with cobalt being a more active phase for decomposition. The H_2O_2 efficiency will be discussed later.

The yield of β-pinene epoxide with all catalysts based on MCM-41 (Fig. 8.B), except CuM1 and CoM1, exhibited maximum values of ca. 80–83 % at 2 h, whereas CuM1 showed the maximum value of 49 % at 24 h. On the other hand, Fig. 9.B shows similar maximum values of the yield of epoxide with all materials, except Fe-modified catalysts (FeS1 and FeS2) which showed their maximum yields at 7 h corresponding to 76 % and 80 %, respectively. Cobalt-based catalysts are not active in the reaction, which causes the yield of epoxide to be zero. The blank test (Fig. 8.B and 9.B) demonstrated a 50 % yield of epoxide at 48 h, explaining the necessity of using an acidic material, either MCM-41, SBA-15, or metal-modified support to promote the rearrangement of the epoxide towards isomers. In the case of catalysts based on MCM-41 (Fig. 8.B), yield of epoxide of ca. 2.5 %, 6.4 %, 10.2 %, and 16.0 % were reached at 48 h with MCM-41, SnM2, SnM1, and FeM1, respectively, whereas with catalysts based on SBA-15 (Fig. 9.B), yield of epoxide of 0 %, 5.3 %, 7.3 %, 12.2 %, and 20.5 % were achieved with SBA-15, FeS1, FeS2, SnS2, and CuS1, respectively. Surprisingly, the yield to epoxide at 48 h with SnS1 catalyst is like the blank test. It is noteworthy that the yield (or selectivity) to epoxide decreases as the reaction progresses, explained by the formation of its main isomers like *cis/trans*-myrtanal and perillyl alcohol, and suggested hydration of the epoxide to a diol ($C_{10}H_{18}O_2$) represented by the product 6 (section 7, Supporting Information).

With MCM-41 prepared catalysts (Fig. 8.C), the materials MCM-41, SnM1, SnM2, and FeM1 exhibited higher yields of myrtanal ranging from 50 to 53 % after 48 h, compared with 38 %, 29 %, and 0 % associated with the blank, CuM1, and CoM1, respectively. In the case of SBA-15 materials (Fig. 9.C), catalysts impregnated with Fe (FeS1 and FeS2) significantly demonstrated the highest yields of myrtanal at 48 h with values of 62.3 % and 59.0 %, respectively, in comparison with the other catalysts with values between 35 % and 45 % for SnS2, FeS1, and SBA-15. Notice that CuS1 presented a very low yield of myrtanal of ca. 15 %, lower than the analogous material based on MCM-41. These results are consistent with previous yields of β-pinene epoxide, which means the yield of myrtanal increases as the yield to epoxide decreases, intrinsically explained by the consecutive isomerization reaction of the epoxide (Fig. 1). Additionally, the findings underscore the limitations of Cu and Co as active phases for achieving highly selective transformation towards myrtanal as the target molecule. However, an active phase is required to further enhance the yield of myrtanal, observing favoring

this target product with Fe and Sn materials.

The yield of perillyl alcohol, another typical product resulting from the rearrangement of β-pinene epoxide, varies between 0 % and 10 %, as depicted in Fig. 8.D and Fig. 9.D. The highest yields (6–10 %) are attained with longer reaction times using materials containing Sn (SnM1, SnM2, SnS2) and Fe (FeM1, FeS1, FeS2) as active phases. Conversely, Cu-modified catalysts yield perillyl alcohol in amounts lower than 5 % throughout the entire reaction time. Some literature reports using heterogeneous catalysts based on Fe and Sn have shown the production of perillyl alcohol. For instance, Sn-MCM-41 achieved a yield of 65 % at 70 °C over 24 h using dimethylsulfoxide (DMSO) as a solvent [28], while Fe-β zeolite yielded 63 % at 70 °C over 3 h, also in DMSO [29]. The authors attributed the enhanced selectivity to perillyl alcohol to the presence of a strong basic polar solvent like DMSO.

The *cis/trans*-myrtanal molar ratio reaches a maximum of ca. 2.0 in the absence of a catalyst (Blank) after 24 h, as depicted in Fig. 8.E and 9. E. Similarly, with mesoporous materials such as MCM-41 (Fig. 8.E) and SBA-15 (Fig. 9.E), a very similar maximum was achieved within the same time. With Sn and Fe-modified catalysts, a positive trend is observed over time, resulting in molar ratios between 1.5 and 2.0 at 48 h with MCM-41-based catalysts (Fig. 8.E) and between 1.8 and 2.3 at 48 h with SBA-15-based catalysts (Fig. 9.E). Conversely, Cu-modified catalysts exhibited molar ratios between 2.5 and 2.9 at 48 h. Our results demonstrate that *cis*-myrtanal is preferred over *trans*-myrtanal, regardless of the heterogeneous catalyst used. Although, typically in aldehydes, the *trans* configuration can be more stable than the *cis* configuration due to steric hindrance and electronic effects, as the larger groups in the *trans* configuration are farther apart, our results indicate that under the reaction conditions, the *cis* isomer is more kinetically favored than the *trans* isomer. These findings are novel, as there is no existing knowledge of other studies reporting the preference of myrtanal isomers.

Figure S41.A and Fig. S42.A illustrate the yield of myrtanal as a function of the yield of β-pinene epoxide for materials based on MCM-41 and SBA-15, respectively. From those results is concluded the consecutive reactions of epoxidation and isomerization, as the yield of myrtanal increases with the decrease in the yield of epoxide, signifying its ring opening. Similarly, Figure S41.B and Fig. S42.B show that diol (product 6, $C_{10}H_{18}O$) is formed as β-pinene epoxide disappears in the reaction. The investigation to determine precisely whether diol is obtained from the hydration of epoxide, as previously reported for limonene-1,2-epoxide [66], or from an intermediate like the other products mentioned in the Supporting Information, is beyond the scope of our study.
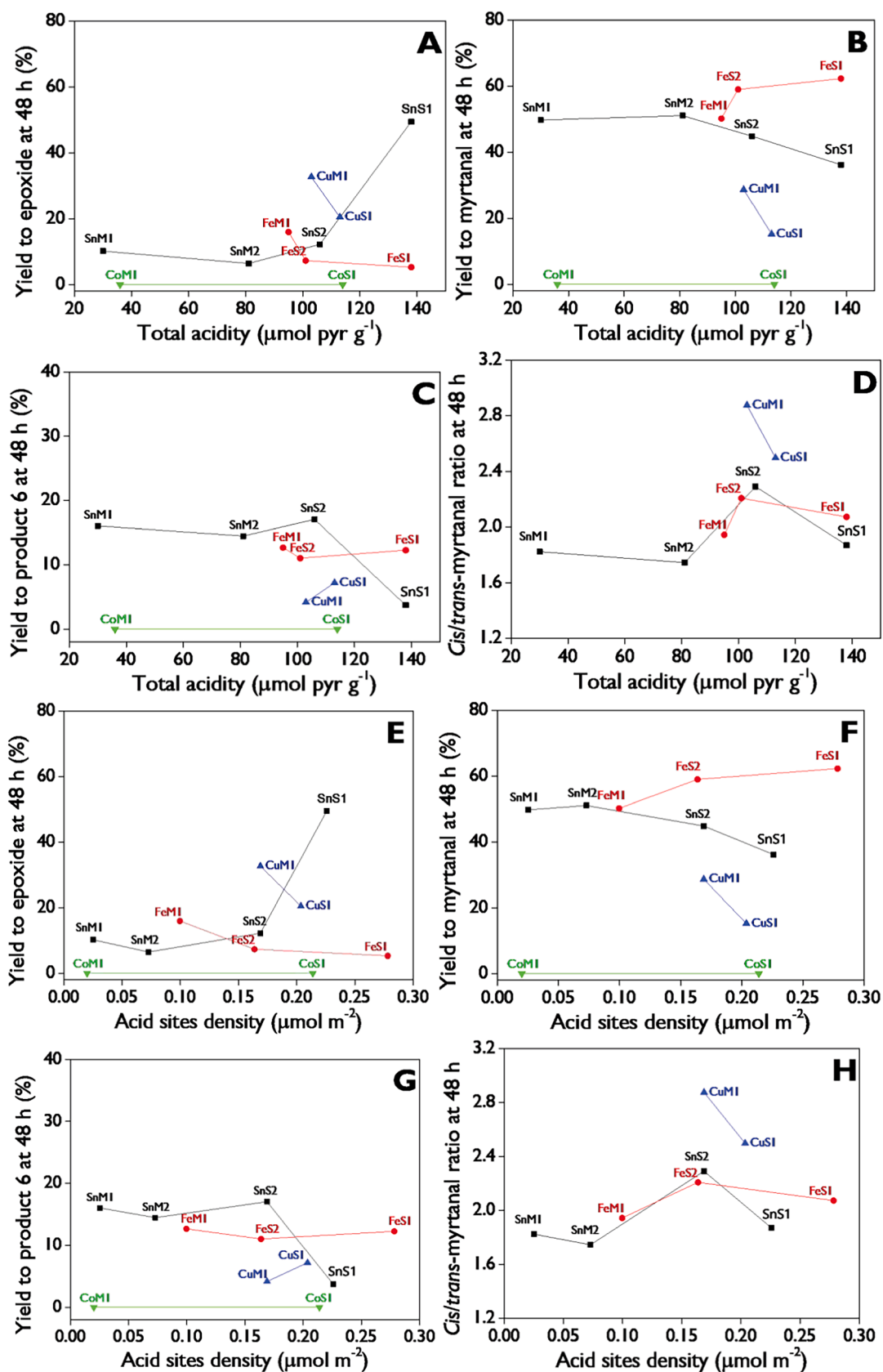
Fig. 11. Total acidity (**A, B, C, D**) and acid sites density (**E, F, G, H**) as descriptors of yield of epoxide (**A, E**), yield of myrtanal (**B, F**), yield of product 6 (**C, G**), and *cis/trans*-myrtanal molar ratio (**D, H**). **Reaction conditions:** 0.1 mmol of β-pinene with weight ratios of 1: 0.72: 1.2: 30.3: 19.7: 15.7: 0.8 for β-pinene: acidic catalyst: MgO: H_2O: acetone: acetonitrile: H_2O_2, 50 °C, 1000 rpm.
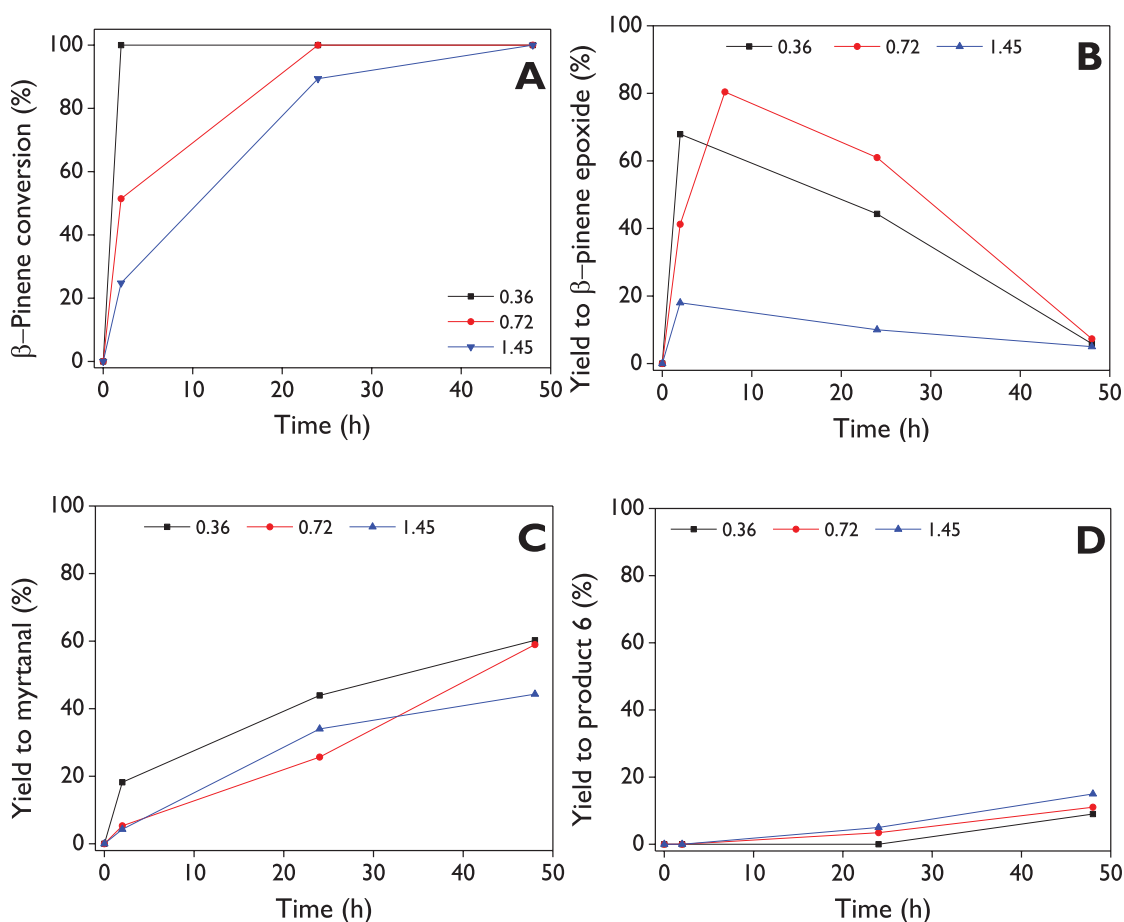
Fig. 12. Effect of amount of FeS2 in the one-pot transformation of β-pinene: **(A)** β-Pinene conversion, **(B)** yield of β-pinene epoxide, **(C)** yield of myrtanal, **(D)** yield of product 6. **Reaction conditions:** 0.1 mmol of β-pinene with weight ratios of 1: (0.36, 0.72, 1.45): 1.2: 30.3: 19.7: 15.7: 0.8 for β-pinene: acidic catalyst: MgO: H_2O: acetone: acetonitrile: H_2O_2, 50 °C, 1000 rpm.

3.2.3. Conversion and efficiency of the oxidizing agent

The profiles of H_2O_2 conversion (Figure S43) were determined using the mathematical procedure outlined in our recent work [66], employing the global conversion of H_2O_2 calculated via cerimetric titration. These profiles effectively demonstrate that the reaction rate of H_2O_2 decomposition follows the sequence: Co > Cu > Fe > Sn, whether supported on MCM-41 (Figure S43.B) or SBA-15 (Figure S43.D). Additionally, the H_2O_2 efficiency [66] for materials based on MCM-41 (Fig. 10.A) and SBA-15 (Fig. 10.B) indicate that efficiency is null for cobalt-based catalysts, whereas for Sn-modified catalysts, nearly 100 % efficiency can be achieved within 2 h, albeit decreasing with an increase in the reaction time. Therefore, Sn emerges as a promising metal for substantially mitigating the decomposition of H_2O_2, consistent with recent studies utilizing Sn-dealuminated zeolite Y for the efficient epoxidation of R-(+)-limonene [66], reaching efficiency values up to 85 %, demonstrating that most of the consumption of H_2O_2 is directed towards the production of the corresponding epoxide. It is noteworthy that with the blank test, efficiency remains consistently high throughout the entire reaction time, as expected due to the absence of metal species promoting decomposition. On the other hand, although Sn yielded the highest efficiency among the various active phases, the results with Fe are also promising. This is particularly notable considering that catalysts based on Fe anchored on SBA-15 showed the highest yields of myrtanal.

3.2.4. Acidity-based properties as descriptors of the catalytic activity

The Lewis acid sites play a crucial role in the highly selective synthesis of target products such as myrtanal through the ring-opening of β-pinene epoxide. Therefore, understanding the dependency of catalytic

data, such as activity in terms of conversion and selectivity to rearrange products, on total acidity (specifically, Lewis acidity) and acid site density is of great interest. Recently, acid site density has been identified as a suitable kinetic descriptor for catalytic reactions employing microporous materials like zeolites [87] and mesoporous materials [88]. Fig. 11.A shows that the yield of β-pinene epoxide increases as total acidity increases for Sn-modified catalysts, reaching a yield of ca. 49 % after 48 h with the SnS1 catalyst possessing a total acidity of 138 μmol g^{-1}. Conversely, with Fe-modified catalysts, epoxide yield decreases as total acidity increases, reaching a minimum value of 5.3 % with FeS1, which has a similar acidity to SnS1. These results suggest the critical role of the active phase in the one-pot tandem route, as the catalytic behavior is entirely dependent on the impregnated metal on the mesoporous supports. Cu-based catalysts exhibit a similar inverse relationship between the yield of epoxide and total acidity, resembling the behavior of Fe-based catalysts. However, Co-based catalysts show no activity in the catalytic reaction, as evidenced by the null efficiency of H_2O_2 shown in Fig. 10.

The relationship between the yield of myrtanal at 48 h and total acidity (Fig. 11.B) shows an opposite profile to the yield of epoxide for materials impregnated with Sn and Fe. This can be explained by the consecutive reactions where the epoxide is formed first and subsequently myrtanal is obtained from the ring-opening of the epoxide. It is noteworthy that the yield of myrtanal decreases as the concentration of acid sites increases with Sn-based catalysts, consistent with previous reports on Sn-modified beta zeolites [26]. Conversely, authors using Fe-based catalysts [45] starting from β-pinene epoxide reported no significant differences in selectivity to myrtanal, whereas in our contribution

Table 7
Heterogeneous catalysts for the isomerization of β-pinene epoxide.

Entry	Catalyst	Solvent	Reaction conditions	Conversion (%)	Selectivity (%)	Ref
1*	MgO – FeS1	Acetone + acetonitrile	0.1 mmol of β-pinene, weight ratios of 1: 0.72: 1.2: 30.3: 19.7: 15.7: 0.8 for β-pinene: acidic catalyst: MgO: H_2O: acetone: acetonitrile: H_2O_2, 50 °C, 1000 rpm	100	5.3 epoxide 42.0 *cis*-myrtanal 20.3 *trans*-myrtanal 2.8 myrtenol 6.3 PA 12.3 diol	This work
2	Fe/MCM-41	Acetonitrile	0.25 mmol substrate, 26 % of catalyst, 1 mL solvent, 70 °C, 1 h	23	90 myrtanal 8 PA 2 myrtenol	[91]
3	Fe/SBA-15	Hexane		27	68 myrtanal 26 PA 6 myrtenol	
4	Sn-Beta-300	Toluene	0.012 mol/L, 75 mg of catalyst, 150 mL total, 70 °C, 6 h	72	66 myrtanal 10 PA 2 myrtenol	[26]
5	Zeolite beta 25	DMSO	0.8 mL substrate, 25 wt% of catalyst (based on the substrate), volume ratio substrate: solvent = 1:5, 70 °C, 2 h	100	19 myrtanal 36 PA 10 myrtenol 9p-Menth-1-en-7,8-diol	[92]
6	Ti/SBA-15	Hexane	0.25 mmol substrate, 10 mg catalyst, 0.5 mL solvent, 80 °C, 1 h	> 99	20 myrtanal 45 PA	[93]
7	Mo/SBA-15	Hexane		> 99	63 PA	
8	Mo/MCM-41	Hexane		98	2 myrtanal 20 PA 5 myrtenol	
9	Mo/SiO$_2$	Hexane		99	12 myrtanal 32 PA 2 myrtenol	
10	Sn-MCM-41	DMSO	1.4 mol/L, 10 wt% of catalyst, volume ratio epoxide: solvent = 1:8, 70 °C, 24 h	98.4	8.2 myrtanal 66.1 PA 12 myrtenol	[28]
11	Fe-β zeolite	DMSO	1.6 mol/L, 10 wt% of catalyst, volume ratio epoxide: solvent = 1:8, 70 °C, 3 h	100	63.1 PA	[29]

PA: Perillyl alcohol.

* This system corresponds to the one-pot transformation of β-pinene towards myrtanal as the major product.

clear differences can be observed in Fig. 11.B. Surprisingly, Cu-based catalysts show a decrease in the yield of myrtanal as total acidity increases, similar to the behavior of epoxide yield. The low yield of myrtanal with these materials, as depicted in Fig. 8.C and 9.C, can explain the behaviors observed in Fig. 11.A and 11.B. Furthermore, these results suggest that Cu materials may not be promising for the proposed one-pot tandem system, as it was previously proposed for a typical isomerization system starting from high-purity epoxide as substrate [45].

The yield of diol at 48 h (Fig. 11.C) shows slight dependence on total acidity in Fe-based catalysts, with values between 11–12.5 %; while values between 14 and 17 % are observed with Sn catalysts in the range of 30–100 μmol pyridine g^{-1}. When the total acidity increases within this range, the yield of diol decreases to 3.7 %. With Cu catalysts, yields between 4 and 7 % were achieved with total acidity between 100 and 120 μmol g^{-1}. The *cis/trans*-myrtanal molar ratio at 48 h (Fig. 11.D) showed the maximum value for all materials at very similar total acidity levels of 100–110 μmol g^{-1}, resulting in a ratio of 2.88 for CuM1 as the global maximum.

Although total acidity in mesoporous catalysts is significant, surface area is also a crucial physicochemical property in heterogeneous catalytic reactions, as it directly relates to the availability of active sites for the reaction to proceed. The surface area is often affected by the type of impregnated metal and the loading, as previously discussed. Therefore, correlating this property with total acidity to calculate a robust kinetic descriptor factor like acid site density (μmol m^{-2}), as reported in Table 5, could be very insightful. Fig. 11.E–11.H exhibit the yield of epoxide, myrtanal, and diol, and the *cis/trans*-myrtanal molar ratio after 48 h as a function of the acid site density, resulting in similar trends as reported in Fig. 11.A-11.D. FeS1, the catalyst with the highest yield of

myrtanal (63 %), presented an acid site density of 0.28 μmol m^{-2}; furthermore, this catalyst presented a total acidity of 138 μmol g^{-1}, a Fe loading of 5.07 %, a BET surface area of 496 m^2 g^{-1}, a pore volume of 0.96 cm^3 g^{-1}, an average pore size of 6.37 nm, and a metal coverage (MC) of 1.10 entities nm^{-2}. It is noteworthy that this material presented the highest MC (Table 3) and total acidity (Table 5), and the lowest BET surface area (Table 3).

3.2.5. Effect of the reaction conditions

The reaction conditions, based on weight ratios for substrate: MgO: H_2O: acetone: acetonitrile: H_2O_2, have been previously investigated using β-pinene [17] and limonene [18] as substrates. Therefore, the best conditions for those parameters have been employed in this contribution. Here, the amount of FeS2 in the one-pot reaction of β-pinene is evaluated by varying the FeS2: β-pinene weight ratio between 0.36 and 1.45. Fig. 12.A confirms that the presence of a large amount of the acid catalyst in the reaction medium hampers the substrate conversion, attributed to favoring the decomposition of H_2O_2 (Fig. 10) [89], obtaining complete conversions more rapidly with only 0.36 of weight ratio. Figure S45.A demonstrates that the overall conversion of H_2O_2 increases with the increase in the amount of FeS2. Additionally, Figure S45.B shows a linear trend between the initial reaction rate of H_2O_2 and the catalyst mass, confirming the absence of mass transfer limitations. The yield of epoxide (Fig. 12.B) reaches its maximum at short reaction times for the different ratios, with complete consumption of epoxide at long times. During this extended period, it is principally converted to myrtanal (Fig. 12.C) but also to diol (product 6, Fig. 12.D). Diol is slightly favored with high amounts of acid catalyst (high weight ratios), which, in turn, reduces the selectivity towards myrtanal as the
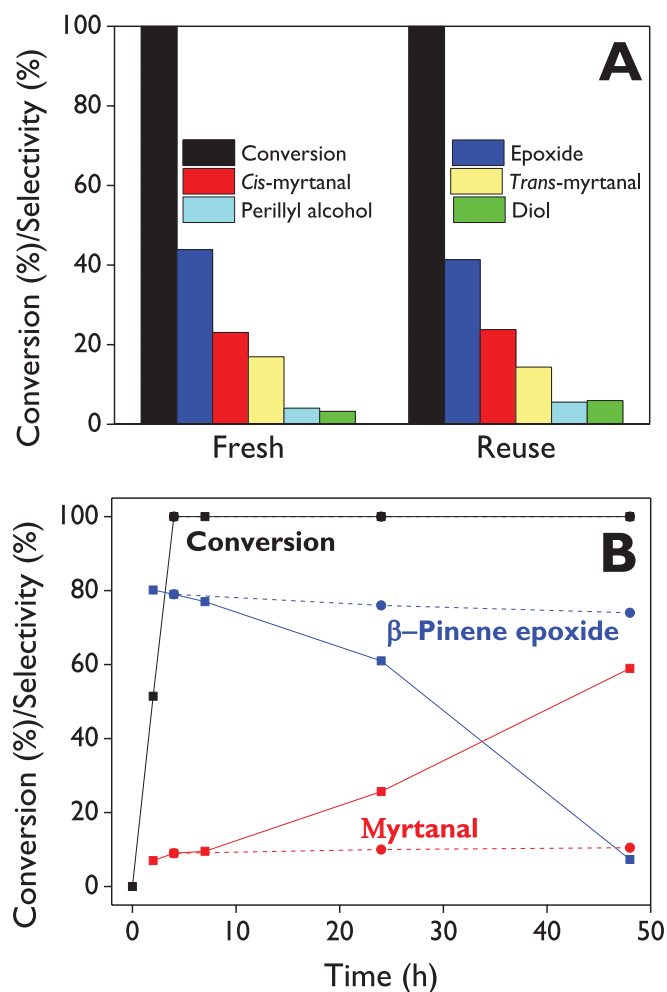
Fig. 13. Stability of FeS2 catalyst in the one-pot transformation of β-pinene: **(A)** β-Pinene conversion and selectivity for the fresh and reuse runs after 20 h, **(B)** β-Pinene conversion and selectivity as function of time for fresh run (solid lines) and leaching test (dashed lines), where catalyst was removed at 4 h. **Reaction conditions:** 0.1 mmol of β-pinene with weight ratios of 1: 0.72: 1.2: 30.3: 19.7: 15.7: 0.8 for β-pinene: acidic catalyst: MgO: H_2O: acetone: acetonitrile: H_2O_2, 50 °C, 1000 rpm.

target molecule. Figures S44.A and B illustrate the yield of myrtanal and the yield of diol as function of the yield of β-pinene epoxide, respectively. They demonstrate the consecutive reactions of epoxidation and isomerization.

The effect of H_2O_2 concentration (H_2O_2/β-pinene weight ratio) has been previously investigated in our research group for this system [90], demonstrating that 0.80 is the most suitable ratio, favoring the yield of myrtanal. Additionally, the effect of temperature was evaluated, showing the inherent behavior of increasing catalytic activity (conversion) with temperature. However, results showed that the best selectivity to myrtanal was achieved at 50 °C, which avoids the formation of many products compared to higher temperatures such as 60 and 70 °C. This is advantageous due to the low energy requirements in the system.

3.2.6. Scope of the one-pot tandem catalytic system

The results of this contribution demonstrated the significance of the proposed one-pot tandem catalytic system for the highly selective synthesis of myrtanal as the major product, forming a mixture of *cis + trans* isomers, in comparison with other heterogeneous catalysts (Table 7) utilized solely for the second step of the epoxide isomerization. With the one-pot tandem system (entry 1), a yield of 62.3 % of myrtanal can be achieved starting from β-pinene, which markedly surpasses previous

catalysts reported, including Sn-Beta-300 (entry 4), which yielded myrtanal at approximately 47.5 %. This promising catalytic activity achieved with our one-pot tandem system is noteworthy as it demonstrates the establishment of compatible and mild reaction conditions for the one-pot transformation of β-pinene, including very low temperature (50 °C), benign solvents and reagents like acetone and acetonitrile, and a green oxidizing agent such as H_2O_2. Conversely, very poor yields of myrtanal were obtained with the other catalysts (entries 2–3, 5–11). These results lead to the conclusion regarding the synergistic effect between the Payne system for the synthesis of β-pinene epoxide and subsequent isomerization, selectively promoting myrtanal formation by acidic catalysts like FeS1 (Fe/SBA-15).

3.3. Catalyst stability

The robustness of the FeS2 catalyst was explored through reusability and leaching tests. For the reuse tests, the catalyst was separated from the reaction medium by centrifugation (3000 rpm, 8 min) for subsequent washing with acetone at 50 °C and drying at 100 °C [18]. The β-pinene conversion and selectivity to products after 20 h of reaction are shown in Fig. 13.A. The results demonstrated that catalytic activity is completely recovered after washing and drying, showing complete conversion. Selectivity to target products remains approximately constant between the fresh and reuse runs, with values ranging between 41–44 % for epoxide and 38–40 % for myrtanal.

The leaching test was conducted using the hot-filtration method to remove the mixture of catalysts (MgO+FeS2) after 4 h of reaction. Fig. 13.B shows that profiles, when catalysts were removed (dashed lines), did not significantly change between 4 and 48 h, demonstrating the heterogeneity of the reaction.

3.4. Plausible reaction pathway

The Payne system has been successfully reported for the epoxidation route of monoterpenes [17,18] which involves the formation of an active intermediate oxidant like peroxyacetimidic acid, which is formed by activating H_2O_2 with acetonitrile through a nucleophilic attack by perhydroxyl anion species (HOO^-) on the nitrile [94,95]. Furthermore, the MgO material contains medium-strength basic sites, which favors the epoxidation route of β-pinene [17]. Fig. 14 shows the proposed reaction pathway for the one-pot tandem transformation of β-pinene using two heterogeneous catalysts: MgO and Fe/support, based on a mechanism previously reported by our research group [17].

Initially, the presence of basic sites in MgO, along with deprotonation − favored by a basic pH in the system − and the rehydration of MgO, facilitate the formation of the epoxidation agent, namely peroxyacetimidic acid. Subsequently, the substrate undergoes activation on Mg^{2+} sites via the exocyclic carbon–carbon double bond and reacts with the epoxidation agent, resulting in the formation of β-pinene epoxide and acetamide. Furthermore, a relatively low yield of myrtanal was observed, attributed to the thermal effect in the rearrangement of the epoxide. Then, the *exo*-epoxide adsorbs and coordinates onto the Lewis acid site (Fe^{3+}) of Fe/MCM-41 or Fe/SBA-15 materials, which are widely known to favor the ring opening towards myrtanal, leading to iron reduction, cleavage of the C-O bond, and formation of the tertiary carbocation. Subsequently, hydrogen transfer facilitates the formation of the secondary carbocation at the *exo*-carbon until the lone pair of electrons from the oxygen coordinated to iron neutralizes the carbocation charge, resulting in the formation of a C=O bond [45]. Finally, myrtanal, the desired product, is synthesized, and the acid catalyst is regenerated.

4. Conclusions

A Payne system consisting of commercial MgO with an acid catalyst was used to evaluate the one-pot transformation of β-pinene using a
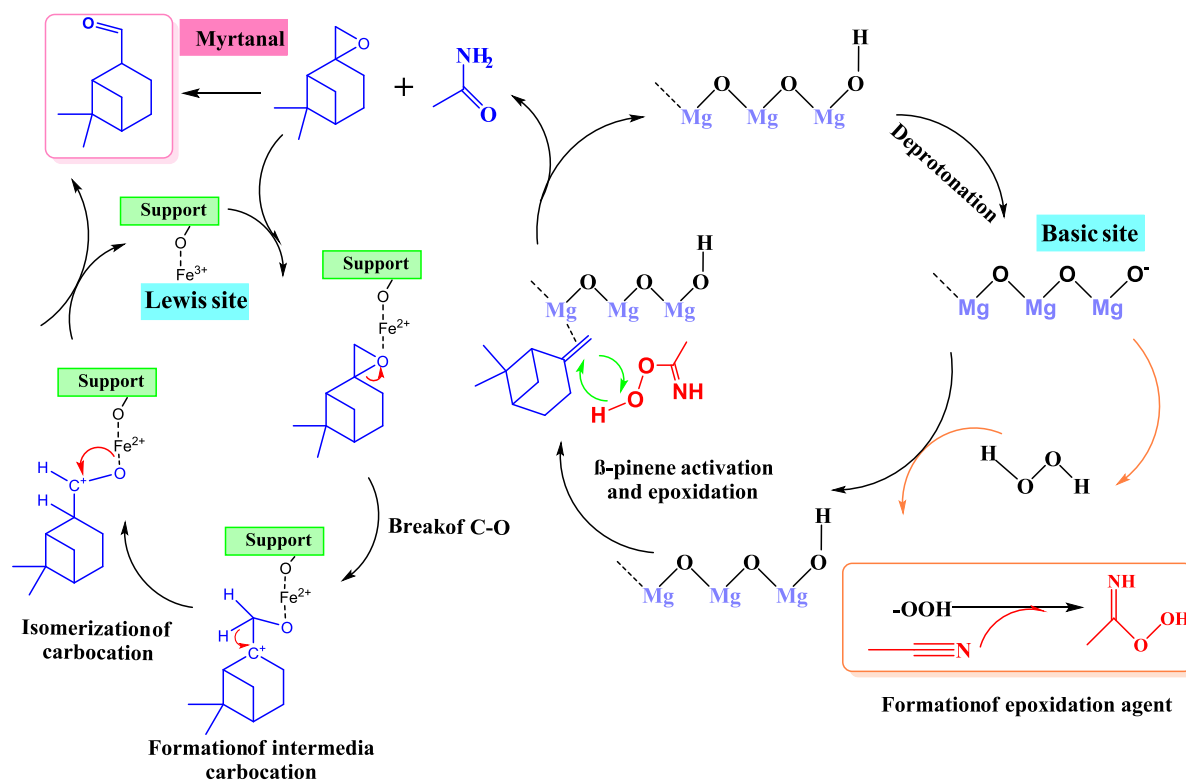
Fig. 14. Plausible reaction pathway for the synthesis of myrtanal through a one-pot tandem route of β-pinene.

catalysis-in-tandem approach. The aim was to synthesize β-pinene epoxide through the oxidation of β-pinene with H_2O_2, followed by isomerization towards a mixture of myrtanal isomers as the target products. The acid catalysts were based on mesoporous supports such as MCM-41 and SBA-15, modified with various metals (Sn, Fe, Cu, Co) using the wetness impregnation method. The synthesized products are widely employed as fine chemicals in fragrances, flavors, and precursors for pharmaceuticals.

The synthesized catalysts exhibited typical ordered mesoporous structures, as confirmed by XRD, although some degree of loss in crystallinity was noted after the anchoring of metals. All catalysts showed typical type-IV isotherms; however, some lacked the characteristic hysteresis loop, attributed to low pore sizes at the boundary between micro- and mesopores. The BET surface area decreased as the metal loading increased in all materials. Channels with ordered hexagonal arrays were observed for all catalysts through TEM, except for cobalt-modified MCM-41, which correlated with a low-intensity peak in XRD. TEM micrographs suggested the presence of Sn on the support surface, while for Fe- and Cu-based catalysts, the metal nanoparticles were located inside the channels. The wetness impregnation method achieved excellent distribution of metals on the supports, as demonstrated by the metal mapping. All materials exhibited solely Lewis acid sites, as indicated by the band at 1450 cm^{-1} in pyridine-FTIR analysis.

The highest yields of myrtanal (59.0–62.3 %) were obtained with Fe-SBA-15 materials after 48 h at 50 °C, using weight ratios of 1: 0.72: 1.2: 30.3: 19.7: 15.7: 0.8 for β-pinene: Fe-SBA-15: MgO: H_2O: acetone: acetonitrile: H_2O_2. High concentrations of H_2O_2, high amounts of acid catalysts, and high temperatures favored the formation of other products over myrtanal. The total acidity and the acid site density were proposed as suitable descriptors of the catalytic activity, highlighting the crucial role of acidity in the ring opening and selectivity of target products. Fe-SBA-15, with the highest total acidity of 138 $\mu mol\ g^{-1}$ and the highest acid density of 0.28 $\mu mol\ m^{-2}$, exhibited the best yield to myrtanal (62.3 %). This material also presented the highest metal coverage of 1.10 entities nm^{-2}. Cu and Co catalysts showed poor or no activity in the

catalytic reaction due to their high activity in the decomposition of H_2O_2. The robustness of the Fe/SBA-15 catalyst was tested through reusability and leaching tests, resulting in no significant loss of activity and selectivity for myrtanal, nor leaching of Fe as the active phase.

In this study, a plausible reaction pathway was proposed considering MgO for the epoxidation route and Lewis acid site (Fe^{3+}) for the selective ring opening of the epoxide towards myrtanal. Finally, this is the first study of a one-pot tandem system for the synthesis of myrtanal from β-pinene under mild reaction conditions.

CRediT authorship contribution statement

Luis A. Gallego-Villada: Writing – original draft, Methodology, Investigation, Formal analysis, Conceptualization. **Edwin A. Alarcón:** Writing – review & editing, Supervision, Resources, Funding acquisition, Conceptualization. **Felipe Bustamante:** Supervision. **Aída Luz Villa:** Writing – review & editing, Resources.

Declaration of competing interest

The authors declare that they have no known competing financial interests or personal relationships that could have appeared to influence the work reported in this paper.

Data availability

Data will be made available on request.

express his gratitude to the Universidad de Antioquia for its support of his Ph.D. studies through the "Beca Doctoral Universidad de Antioquia" scholarship.

Appendix A. Supplementary data

Supplementary data to this article can be found online at https://doi.org/10.1016/j.jcat.2024.115698.

References

[1] H.-U. Blaser, Heterogeneous catalysis for fine chemicals production, Catal. Today. 60 (2000) 161–165, https://doi.org/10.1016/S0920-5861(00)00332-1.

[2] C. Lucarelli, A. Vaccari, Examples of heterogeneous catalytic processes for fine chemistry, Green Chem. 13 (2011) 1941, https://doi.org/10.1039/c0gc00760a.

[3] J.E. Sánchez-Velandia, L.A. Gallego-villada, P. Mäki-Arvela, A. Sidorenko, D. Y. Murzin, Upgrading biomass to high-added value chemicals: synthesis of monoterpenes-based compounds using catalytic green chemical pathways, Catal. Rev. (2024) 1–126, https://doi.org/10.1080/01614940.2024.2329553.

[4] A. Masyita, R. Mustika Sari, A. Dwi Astuti, B. Yasir, N. Rahma Rumata, T. Bin Emran, F. Nainu, J. Simal-Gandara, Terpenes and terpenoids as main bioactive compounds of essential oils, their roles in human health and potential application as natural food preservatives, Food Chem. x. 13 (2022) 100217, https://doi.org/10.1016/j.fochx.2022.100217.

[5] V. Karuppiah, K.E. Ranaghan, N.G.H. Leferink, L.O. Johannissen, M. Shanmugam, A. Ní Cheallaigh, N.J. Bennett, L.J. Kearsey, E. Takano, J.M. Gardiner, M.W. van der Kamp, S. Hay, A.J. Mulholland, D. Leys, N.S. Scrutton, Structural basis of catalysis in the bacterial monoterpene synthases linalool synthase and 1,8-cineole synthase, ACS Catal. 7 (2017) 6268–6282, https://doi.org/10.1021/acscatal.7b01924.

[6] L.A. Gallego-Villada, E.A. Alarcón, A.L. Villa, Evaluation of nopol production obtained from turpentine oil over Sn/MCM-41 synthesized by wetness impregnation using the Central Composite Design, Mol. Catal. 498 (2020) 111250, https://doi.org/10.1016/j.mcat.2020.111250.

[7] M. Golets, S. Ajaikumar, J.-P. Mikkola, Catalytic upgrading of extractives to chemicals: monoterpenes to "EXICALS", Chem. Rev. 115 (2015) 3141–3169, https://doi.org/10.1021/cr500407m.

[8] H. Zhang, X. Lu, L. Yang, Y. Hu, M. Yuan, C. Wang, Q. Liu, F. Yue, D. Zhou, Q. Xia, Efficient air epoxidation of cycloalkenes over bimetal-organic framework ZnCo-MOF materials, Mol. Catal. 499 (2021) 111300, https://doi.org/10.1016/j.mcat.2020.111300.

[9] A. Corma, S. Iborra, A. Velty, Chemical routes for the transformation of biomass into chemicals, Chem. Rev. 107 (2007) 2411–2502, https://doi.org/10.1021/cr050989d.

[10] D. García, F. Bustamante, A.L. Villa, M. Lapuerta, E. Alarcón, Oxyfunctionalization of turpentine for fuel applications, Energy Fuel 34 (2020) 579–586, https://doi.org/10.1021/acs.energyfuels.9b03742.

[11] A. Corma, M. Renz, M. Susarte, Transformation of biomass products into fine chemicals catalyzed by solid lewis- and brønsted-acids, Top. Catal. 52 (2009) 1182–1189, https://doi.org/10.1007/s11244-009-9266-5.

[12] P. Tao, X. Lu, H. Zhang, R. Jing, F. Huang, S. Wu, D. Zhou, Q. Xia, Enhanced activity of microwave-activated CoOx/MOR catalyst for the epoxidation of α-pinene with air, Mol. Catal. 463 (2019) 8–15, https://doi.org/10.1016/j.mcat.2018.11.006.

[13] H. Martinez Q, Á.A. Amaya, E.A. Paez-Mozo, F. Martinez O, S. Valange, Photo-assisted O-atom transfer to monoterpenes with molecular oxygen and a dioxoMo (VI) complex immobilized on TiO2 nanotubes, Catal. Today. 375 (2021) 441–457, https://doi.org/10.1016/j.cattod.2020.07.053.

[14] H. Guo, X. Lu, J. He, H. Zhang, H. Zhang, J. Dong, D. Zhou, Q. Xia, Co-MOF nanosheet supported on ZSM-5 with an improved catalytic activity for air epoxidation of olefins, Mater. Chem. Phys. 294 (2023) 127001, https://doi.org/10.1016/j.matchemphys.2022.127001.

[15] C. Wang, H. Zhan, X. Lu, R. Jing, H. Zhang, L. Yang, X. Li, F. Yue, D. Zhou, Q. Xia, A recyclable cobalt(III)–ammonia complex catalyst for catalytic epoxidation of olefins with air as the oxidant, New J. Chem. 45 (2021) 2147–2156, https://doi.org/10.1039/D0NJ05466F.

[16] Y. Mahamat Ahmat, S. Madadi, L. Charbonneau, S. Kaliaguine, Epoxidation of terpenes, Catalysts 11 (2021) 847, https://doi.org/10.3390/catal11070847.

[17] D. García, M. Jaramillo, F. Bustamante, A.L. Villa, E. Alarcón, Epoxidation of β-pinene with a highly-active and low-cost catalyst, Brazilian, J Chem. Eng. 38 (2021) 89–100, https://doi.org/10.1007/s43153-020-00078-y.

[18] L.A. Gallego-Villada, E.A. Alarcón, A.L. Villa, Versatile heterogeneous catalytic system for the selective synthesis of limonene epoxide and diepoxide, Ind. Eng. Chem. Res. 62 (2023) 20152–20169, https://doi.org/10.1021/acs.iecr.3c02633.

[19] K. Schröder, K. Junge, A. Spannenberg, M. Beller, Design of a bio-inspired imidazole-based iron catalyst for epoxidation of olefins: mechanistic insights, Catal. Today. 157 (2010) 364–370, https://doi.org/10.1016/j.cattod.2010.04.034.

[20] A.A. de Oliveira, M.L. da Silva, M.J. da Silva, Palladium-catalysed oxidation of bicycle monoterpenes by hydrogen peroxide in acetonitrile solutions: a metal reoxidant-free and environmentally benign oxidative process, Catal. Letters. 130 (2009) 424–431, https://doi.org/10.1007/s10562-009-9970-6.

[21] C.B. Woitiski, Y.N. Kozlov, D. Mandelli, G.V. Nizova, U. Schuchardt, G.B. Shul'pin, Oxidations by the system "hydrogen peroxide–dinuclear manganese(IV)

[22] complex–carboxylic acid", J. Mol. Catal. A Chem. 222 (2004) 103–119, https://doi.org/10.1016/j.molcata.2004.08.003.

[22] J.E. Sánchez-Velandia, L.M. Valdivieso, F. Martínez O, S.M. Mejía, A.L. Villa, J. Wärnå, D.Y. Murzin, Synthesis of trans-pinocarveol from oxidation of β-pinene using multifunctional heterogeneous catalysts, Mol. Catal. 541 (2023), https://doi.org/10.1016/j.mcat.2023.113104.

[23] A. Bordoloi, F. Lefebvre, S.B. Halligudi, Organotin-oxometalate coordination polymer catalyzed oxyfunctionalization of monoterpenes, J. Mol. Catal. A Chem. 270 (2007) 177–184, https://doi.org/10.1016/j.molcata.2007.02.004.

[24] O. de la Torre, M. Renz, A. Corma, Rearrangement of NL-pinene epoxide into myrtanal with well-defined single-site substituted molecular sieves as reusable solid Lewis-acid catalysts, Applied Catal A, Gen. 380 (2010) 165–171, https://doi.org/10.1016/j.apcata.2010.03.056.

[25] A. Corma, M. Renz, O. De La Torre, Production of myrtanal from beta-pinene epoxide, US 8,633,338 B2, 2014.

[26] P. Mäki-Arvela, N. Kumar, S.F. Díáz, A. Aho, M. Tenho, J. Salonen, A.-R. Leino, K. Kordás, P. Laukkanen, J. Dahl, I. Sinev, T. Salmi, D.Y. Murzin, Isomerization of β-pinene oxide over Sn-modified zeolites, J. Mol. Catal. A Chem. 366 (2013) 228–237, https://doi.org/10.1016/j.molcata.2012.09.028.

[27] E. Salminen, L. Rujana, P. Mäki-Arvela, P. Virtanen, T. Salmi, J.-P. Mikkola, Biomass to value added chemicals: isomerisation of β-pinene oxide over supported ionic liquid catalysts (SILCAs) containing Lewis acids, Catal. Today. 257 (2015) 318–321, https://doi.org/10.1016/j.cattod.2014.05.024.

[28] E. Vyskočilová, M. Malý, A. Aho, J. Krupka, L. Červený, The solvent effect in β-pinene oxide rearrangement, React. Kinet. Mech. Catal. 118 (2016) 235–246, https://doi.org/10.1007/s11144-016-0994-9.

[29] E. Vyskočilová, J. Dušek, M. Babirádová, J. Krupka, I. Paterová, L. Červený, Perillyl alcohol preparation from β-pinene oxide using Fe-modified zeolite beta, Res. Chem. Intermed. 44 (2018) 3971–3984, https://doi.org/10.1007/s11164-018-3335-y.

[30] H. Li, J. Liu, J. Zhao, H. He, D. Jiang, S.R. Kirk, Q. Xu, X. Liu, D. Yin, Selective catalytic isomerization of β-pinene oxide to perillyl alcohol enhanced by protic tetraimidazolium nitrate, ChemistryOpen. 10 (2021) 477–485, https://doi.org/10.1002/open.202000318.

[31] M.J. Climent, A. Corma, S. Iborra, Heterogeneous catalysts for the one-pot synthesis of chemicals and fine chemicals, Chem. Rev. 111 (2011) 1072–1133, https://doi.org/10.1021/cr1002084.

[32] Y. Hayashi, Pot economy and one-pot synthesis, Chem. Sci. 7 (2016) 866–880, https://doi.org/10.1039/C5SC02913A.

[33] B. Sundaravel, C.M. Babu, R. Vinodh, W.S. Cha, H.-T. Jang, Synthesis of campholenic aldehyde from α-pinene using bi-functional PrAlPO-5 molecular sieves, J. Taiwan Inst. Chem. Eng. 63 (2016) 157–165, https://doi.org/10.1016/j.jtice.2016.02.028.

[34] D.R. Godhani, H.D. Nakum, D.K. Parmar, J.P. Mehta, N.C. Desai, Zeolite Y encaged Ru(III) and Fe(III) complexes for oxidation of styrene, cyclohexene, limonene, and α-pinene: an eye-catching impact of H2SO4 on product selectivity, J. Mol. Catal. A Chem. 426 (2017) 223–237, https://doi.org/10.1016/j.molcata.2016.11.020.

[35] C.M. Chanquía, A.L. Cánepa, E.L. Winkler, E. Rodríguez-Castellón, S.G. Casuscelli, G.A. Eimer, Nature of active vanadium nanospecies in MCM-41 type catalysts for olefins oxidation, Mater. Chem. Phys. 175 (2016) 172–179, https://doi.org/10.1016/j.matchemphys.2016.03.014.

[36] P.A. Robles-Dutenhefner, M.J. da Silva, L.S. Sales, E.M.B. Sousa, E.V. Gusevskaya, Solvent-free liquid-phase autoxidation of monoterpenes catalyzed by sol–gel Co/SiO2, J. Mol. Catal. A Chem. 217 (2004) 139–144, https://doi.org/10.1016/j.molcata.2004.03.007.

[37] Y.-W. Suh, N.-K. Kim, W.-S. Ahn, H.-K. Rhee, Redox-mesoporous molecular sieve as a bifunctional catalyst for the one-pot synthesis of campholenic aldehyde from α-pinene, J. Mol. Catal. A Chem. 174 (2001) 249–254, https://doi.org/10.1016/S1381-1169(01)00192-3.

[38] Y.-W. Suh, N.-K. Kim, W.-S. Ahn, H.-K. Rhee, One-pot synthesis of campholenic aldehyde from α-pinene over Ti-HMS catalyst II: effects of reaction conditions, J. Mol. Catal. A Chem. 198 (2003) 309–316, https://doi.org/10.1016/S1381-1169(02)00733-1.

[39] M.J. Climent, A. Corma, S. Iborra, M.J. Sabater, Heterogeneous catalysis for tandem reactions, ACS Catal. 4 (2014) 870–891, https://doi.org/10.1021/cs401052k.

[40] T.L. Lohr, T.J. Marks, Orthogonal tandem catalysis, Nat. Chem. 7 (2015) 477–482, https://doi.org/10.1038/nchem.2262.

[41] M. Grün, K.K. Unger, A. Matsumoto, K. Tsutsumi, Novel pathways for the preparation of mesoporous MCM-41 materials: control of porosity and morphology, Microporous Mesoporous Mater. 27 (1999) 207–216, https://doi.org/10.1016/S1387-1811(98)00255-8.

[42] P. Shah, A.V. Ramaswamy, K. Lazar, V. Ramaswamy, Synthesis and characterization of tin oxide-modified mesoporous SBA-15 molecular sieves and catalytic activity in trans-esterification reaction, Appl. Catal. A Gen. 273 (2004) 239–248, https://doi.org/10.1016/j.apcata.2004.06.039.

[43] G. Jura, W.D. Harkins, Surfaces of solids. XI. determination of the decrease (π) of free surface energy of a solid by an adsorbed film, J. Am. Chem. Soc. 66 (1944) 1356–1362, https://doi.org/10.1021/ja01236a046.

[44] C.A. Emeis, Determination of integrated molar extinction coefficients for infrared absorption bands of pyridine adsorbed on solid acid catalysts, J. Catal. 141 (1993) 347–354, https://doi.org/10.1006/jcat.1993.1145.

[45] J.E. Sánchez-Velandia, A.L. Villa, Isomerization of α- and β- pinene epoxides over Fe or Cu supported MCM-41 and SBA-15 materials, Appl. Catal. A Gen. 580 (2019) 17–27, https://doi.org/10.1016/j.apcata.2019.04.029.

[46] J.S. Beck, J.C. Vartuli, W.J. Roth, M.E. Leonowicz, C.T. Kresge, K.D. Schmitt, C.T. W. Chu, D.H. Olson, E.W. Sheppard, S.B. McCullen, J.B. Higgins, J.L. Schlenker,

A new family of mesoporous molecular sieves prepared with liquid crystal templates, J. Am. Chem. Soc. 114 (1992) 10834–10843, https://doi.org/10.1021/ja00053a020.

[47] A. Galarneau, H. Cambon, F. Di Renzo, R. Ryoo, M. Choi, F. Fajula, Microporosity and connections between pores in SBA-15 mesostructured silicas as a function of the temperature of synthesis, New J. Chem. 27 (2003) 73–79, https://doi.org/10.1039/b207378c.

[48] L.A. Gallego-Villada, E.A. Alarcón, A.L. Villa, Effect of colombian raw materials on the prins condensation reaction over Sn/MCM-41, Catal. Today. 372 (2021) 36–50, https://doi.org/10.1016/j.cattod.2020.10.040.

[49] X. Dong, Y. Wang, H. Dan, Z. Hong, K. Song, Q. Xian, Y. Ding, A facile route to synthesize mesoporous SBA-15 silica spheres from powder quartz, Mater. Lett. 204 (2017) 97–100, https://doi.org/10.1016/j.matlet.2017.05.115.

[50] N.A. Razik, Frecise lattice constant determination of hexagonal, rhombohedral, and tetragonal crystals from X-ray powder diffractometric data, Phys. Status Solidi. 90 (1985) K125–K128, https://doi.org/10.1002/pssa.2210900247.

[51] Y. Ishii, Y. Nishiwaki, A. Al-zubaidi, S. Kawasaki, Pore size determination in ordered mesoporous materials using powder X-ray diffraction, J. Phys. Chem. c. 117 (2013) 18120–18130, https://doi.org/10.1021/jp4057362.

[52] R.J. Farrauto, M.C. Hobson, Catalyst characterization, Encycl. Phys. Sci. Technol., Elsevier (2003) 501–526, https://doi.org/10.1016/B0-12-227410-5/00087-9.

[53] G. Ertl, H. Knozinger, F. Schuth, J. Weitkamp, Handbook of Heterogeneous Catalysis, Wiley-VCH Verlag GmbH, Germany, 2008. 10.1002/9783527610044.

[54] K.S.W. Sing, Reporting physisorption data for gas, solid systems with special reference to the determination of surface area and porosity (Recommendations 1984), Pure Appl Chem. 57 (1985) (1984) 603–619, https://doi.org/10.1351/pac198557040603.

[55] F. Rouquerol, J. Rouquerol, K. Sing, CHAPTER 1 - Introduction, in: F. Rouquerol, J. Rouquerol, K.B.T.-A. by P., P.S. Sing (Eds.), Academic Press, London, 1999: pp. 1–26. 10.1016/B978-012598920-6/50002-6.

[56] T. Miyata, A. Endo, T. Ohmori, T. Akiya, M. Nakaiwa, Evaluation of pore size distribution in boundary region of micropore and mesopore using gas adsorption method, J. Colloid Interface Sci. 262 (2003) 116–125, https://doi.org/10.1016/S0021-9797(02)00254-0.

[57] A. Grosman, C. Ortega, Nature of capillary condensation and evaporation processes in ordered porous materials, Langmuir 21 (2005) 10515–10521, https://doi.org/10.1021/la051030o.

[58] K. Quiroz-Estrada, M. Esparza-Schulz, C. Felipe, A Better understanding of the SBA-15 pores filling through textural changes in CMK-3 carbon synthesis and Its CO2: CH4 adsorption selectivity, J. Compos. Sci. 6 (2022) 344, https://doi.org/10.3390/jcs6110344.

[59] T. Heikkilä, J. Salonen, J. Tuura, N. Kumar, T. Salmi, D.Y. Murzin, M.S. Hamdy, G. Mul, L. Laitinen, A.M. Kaukonen, J. Hirvonen, V.-P. Lehto, Evaluation of mesoporous TCPSi, MCM-41, SBA-15, and TUD-1 materials as API carriers for oral drug delivery, Drug Deliv. 14 (2007) 337–347, https://doi.org/10.1080/10717540601098823.

[60] F. Khanmohammadi, B.M. Razavizadeh, E. Fooladi, Application of electrochemical sensor modified by SBA-15 /Fe3O4/polyaniline nanocomposite for determination of tyrosine in milk samples, Sens. Bio-Sensing Res. 42 (2023) 100602, https://doi.org/10.1016/j.sbsr.2023.100602.

[61] D. Gkiliopoulos, I. Tsamesidis, A. Theocharidou, G.K. Pouroutzidou, E. Christodoulou, E. Stalika, K. Xanthopoulos, D. Bikiaris, K. Triantafyllidis, E. Kontonasaki, SBA-15 mesoporous silica as delivery vehicle for rhBMP-2 bone morphogenic protein for dental applications, Nanomaterials 12 (2022) 822, https://doi.org/10.3390/nano12050822.

[62] Y. Liu, S. Yang, C. Shi, L. Pan, X. Zhang, J.-J. Zou, HPW/MCM-41 catalytic Simmons-Smith cyclopropanation of olefins for synthesis of high-energy–density fuel, Chem. Eng. Sci. 283 (2024) 119366, https://doi.org/10.1016/j.ces.2023.119366.

[63] I. Aguas, M.J. Hidalgo, A.L. Villa, E.A. Alarcón, Homolimonenol synthesis over Sn supported mesoporous materials, Catal. Today. 394–396 (2022) 403–413, https://doi.org/10.1016/j.cattod.2021.07.025.

[64] A. Nuri, A. Bezaatpour, M. Amiri, N. Vucetic, J.-P. Mikkola, D.Y. Murzin, Pd nanoparticles stabilized on the cross-linked melamine-based SBA-15 as a catalyst for the mizoroki-heck reaction, Catal. Letters. 152 (2022) 991–1002, https://doi.org/10.1007/s10562-021-03691-9.

[65] P. Demuth, L.A. Gallego-Villada, P. Mäki-Arvela, R. Majidov, Z. Vajglová, N. Kumar, I. Angervo, M. Lastusaari, K. Eränen, D.Y. Murzin, Micro and mesoporous materials based on zeolite Y for the florol synthesis via the prins cyclization of isoprenol, Catal. Today. 433 (2024) 114695, https://doi.org/10.1016/j.cattod.2024.114695.

[66] L.A. Gallego-Villada, P. Mäki-Arvela, N. Kumar, E.A. Alarcón, Z. Vajglová, T. Tirri, I. Angervo, R. Lassfolk, M. Lastusaari, D.Y. Murzin, Zeolite Y-based catalysts for efficient epoxidation of R-(+)-limonene: insights into the structure-activity relationship, Microporous Mesoporous Mater. 372 (2024) 113098, https://doi.org/10.1016/j.micromeso.2024.113098.

[67] B. Chakraborty, B. Viswanathan, Surface acidity of MCM-41 by in situ IR studies of pyridine adsorption, Catal. Today. 49 (1999) 253–260, https://doi.org/10.1016/S0920-5861(98)00431-3.

[68] A. Ramírez, B.L. Lopez, L. Sierra, Study of the acidic sites and their modifications in mesoporous silica synthesized in acidic medium under quiescent conditions, J. Phys. Chem. b. 107 (2003) 9275–9280, https://doi.org/10.1021/jp0351472.

[69] J.M. Ramos, J.A. Wang, S.O. Flores, L.F. Chen, N. Nava, J. Navarrete, J.M. Domínguez, J.A. Szpunar, Ultrasound-assisted synthesis and catalytic activity of mesostructured FeOx/SBA-15 and FeOx/Zr-SBA-15 catalysts for the oxidative

[70] desulfurization of model diesel, Catal. Today. 349 (2020) 198–209, https://doi.org/10.1016/j.cattod.2018.04.059.

[70] M. Stekrova, N. Kumar, P. Mäki-Arvela, O. Ardashov, K. Volcho, N. Salakhutdinov, D. Murzin, Selective preparation of trans-carveol over ceria supported mesoporous materials MCM-41 and SBA-15, Materials (Basel). 6 (2013) 2103–2118, https://doi.org/10.3390/ma6052103.

[71] A.A. El-Rayyes, A.A. Al-Arfaj, U.K.A. Klein, S.A.I. Barri, Acidity of all-silica MCM-41—studied by laser spectroscopy of adsorbed fluorescent probe compounds, Catal. Letters. 97 (2004) 83–90, https://doi.org/10.1023/B:CATL.0000034292.46628.15.

[72] P.R.S. Braga, A.A. Costa, J.L. de Macedo, G.F. Ghesti, M.P. de Souza, J.A. Dias, S.C.L. Dias, Liquid phase calorimetric-adsorption analysis of Si-MCM-41: evidence of strong hydrogen-bonding sites, Microporous Mesoporous Mater. 139 (2011) 74–80, https://doi.org/10.1016/j.micromeso.2010.10.020.

[73] F. Arena, R. Dario, A. Parmaliana, A characterization study of the surface acidity of solid catalysts by temperature programmed methods, Appl. Catal. A Gen. 170 (1998) 127–137, https://doi.org/10.1016/S0926-860X(98)00041-6.

[74] J. Baltrusaitis, C.R. Usher, V.H. Grassian, Reactions of sulfur dioxide on calcium carbonate single crystal and particle surfaces at the adsorbed water carbonate interface, Phys. Chem. Chem. Phys. 9 (2007) 3011, https://doi.org/10.1039/b617697f.

[75] M. Smyrnioti, T. Ioannides, Synthesis of Cobalt-Based Nanomaterials from Organic Precursors, in: Cobalt, InTech, 2017. 10.5772/intechopen.70947.

[76] W. Xia, H. Wang, X. Zeng, J. Han, J. Zhu, M. Zhou, S. Wu, High-efficiency photocatalytic activity of type II SnO/Sn 3 O 4 heterostructures via interfacial charge transfer, CrstEngComm 16 (2014) 6841–6847, https://doi.org/10.1039/C4CE00884G.

[77] ThermoFisher, Thermo Fisher Scientific, X-Ray Photoelectron Spectroscopy Learning Center, (n.d.). https://www.thermofisher.com/co/en/home/materials-science/learning-center/surface-analysis.html (accessed March 25, 2024).

[78] C.D. Wagner, W.M. Riggs, L.E. Davis, J.F. Moulder, Handbook of Xray photoelectron spectroscopy.pdf, Perkin-Elmer Corporation (1979).

[79] M. Stekrova, N. Kumar, A. Aho, I. Sinev, W. Grünert, J. Dahl, J. Roine, S.S. Arzumanov, P. Mäki-Arvela, D.Y. Murzin, Isomerization of α-pinene oxide using Fe-supported catalysts: selective synthesis of campholenic aldehyde, Appl. Catal. A Gen. 470 (2014) 162–176, https://doi.org/10.1016/j.apcata.2013.10.044.

[80] J.E. Sánchez-Velandia, A.L. Villa, Selective synthesis of high-added value chemicals from α-pinene epoxide and limonene epoxide isomerization over mesostructured catalysts: effect of the metal loading and solvent, Catal. Today. 394–396 (2022) 208–218, https://doi.org/10.1016/j.cattod.2021.09.011.

[81] J.M. Lázaro Martínez, E. Rodríguez-Castellón, R.M.T. Sánchez, L.R. Denaday, G.Y. Buldain, V. Campo Dall' Orto, XPS studies on the Cu(I, II)–polyampholyte heterogeneous catalyst: an insight into its structure and mechanism, J. Mol. Catal. A Chem. 339 (2011) 43–51, https://doi.org/10.1016/j.molcata.2011.02.010.

[82] L. Sun, J. Liu, W. Luo, Y. Yang, F. Wang, C. Weerakkody, S.L. Suib, Preparation of amorphous copper - chromium oxides catalysts for selective oxidation of cyclohexane, Mol. Catal. 460 (2018) 16–26, https://doi.org/10.1016/j.mcat.2018.09.007.

[83] A.M. Venezia, X-ray photoelectron spectroscopy (XPS) for catalysts characterization, Catal. Today. 77 (2003) 359–370, https://doi.org/10.1016/S0920-5861(02)00380-2.

[84] J.H. Scofield, Theoretical Photoionization Cross Sections from 1 to 1500 keV, University of California, Livermore, California, 1973.

[85] J.F. Perez-Benito, Copper(II)-catalyzed decomposition of hydrogen peroxide: catalyst activation by halide ions, Monatshefte Für Chemie/chemical Mon. 132 (2001) 1477–1492, https://doi.org/10.1007/s007060170004.

[86] N. Danyliuk, V. Mandzyuk, Hydrogen peroxide decomposition using cobalt ferrite catalyst activated by induction heating, Mol. Cryst. Liq. Cryst. 766 (2023) 100–110, https://doi.org/10.1080/15421406.2023.2222256.

[87] D.Y. Murzin, Acid Site Density as a Kinetic Descriptor of Catalytic Reactions over Zeolites, Chemistry (Easton). 4 (2022) 1609–1623, https://doi.org/10.3390/chemistry4040105.

[88] D.Y. Murzin, Catalytic kinetics in nanoconfined space of acidic micro/mesoporous materials, Chem. Eng. Sci. 294 (2024) 120078, https://doi.org/10.1016/j.ces.2024.120078.

[89] M. Hermanek, R. Zboril, I. Medrik, J. Pechousek, C. Gregor, Catalytic efficiency of iron(III) oxides in decomposition of hydrogen peroxide: competition between the surface area and crystallinity of nanoparticles, J. Am. Chem. Soc. 129 (2007) 10929–10936, https://doi.org/10.1021/ja072918x.

[90] L.A. Gallego-Villada, E.A. Alarcón, Transformation of monoterpenes through one-pot pathways over heterogeneous catalysts, Eng. Transform. (2022) 36–42.

[91] M. Chaves-Restrepo, A. Viloria, J.E. Sánchez-Velandia, A.L. Villa, Effect of reaction conditions and kinetics of the isomerization of β-pinene epoxide to myrtanal in the presence of Fe/MCM-41 and Fe/SBA-15, React. Kinet. Mech. Catal. 135 (2022) 2013–2029, https://doi.org/10.1007/s11144-022-02220-y.

[92] K. Zítová, E. Vyskočilová, L. Červený, Preparation of α-terpineol and perillyl alcohol using zeolites beta, Res. Chem. Intermed. 47 (2021) 4297–4310, https://doi.org/10.1007/s11164-021-04515-6.

[93] M.C. Cruz, J.E. Sánchez-Velandia, S. Causíl, A.L. Villa, Selective synthesis of perillyl alcohol from β-pinene epoxide over ti and mo supported catalysts, Catal. Letters. 151 (2021) 2279–2290, https://doi.org/10.1007/s10562-020-03489-1.

[94] I. Kirm, F. Medina, X. Rodríguez, Y. Cesteros, P. Salagre, J. Sueiras, Epoxidation of styrene with hydrogen peroxide using hydrotalcites as heterogeneous catalysts, Appl. Catal. A Gen. 272 (2004) 175–185, https://doi.org/10.1016/j.apcata.2004.05.039.

[95] K. Yamaguchi, K. Mori, T. Mizugaki, K. Ebitani, K. Kaneda, Epoxidation of α, β-unsaturated ketones using hydrogen peroxide in the presence of basic hydrotalcite catalysts, J. Org. Chem. 65 (2000) 6897–6903, https://doi.org/10.1021/jo000247e.